Nuclear Magnetic Resonance Microscopy

by

Xiao-wu Tang

Submitted to the Department of Nuclear Engineering
in partial fulfillment of the requirements for the degree of

Doctor of Philosophy

at the

MASSACHUSETTS INSTITUTE OF TECHNOLOGY

June 1999

© Massachusetts Institute of Technology 1999. All rights reserved.

Author . . . .
Department of Nuclear Engineering
April 26, 1999

Certified by. . . . .
David G. Cory
Associate Professor
Thesis Supervisor

Read by . . . .
Sow-hsin Chen
Professor
Thesis Reader

Accepted by . . . .
Lawrence Lidsky
Chairman, Department Committee on Graduate Students
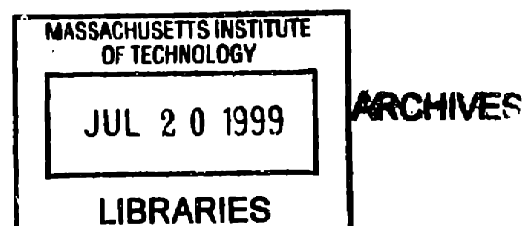
Nuclear Magnetic Resonance Microscopy

by

Xiao-wu Tang

Submitted to the Department of Nuclear Engineering
on April 26, 1999, in partial fulfillment of the
requirements for the degree of
Doctor of Philosophy

Abstract

This thesis describes the design and applications of an improved Nuclear Magnetic Resonance (NMR) microscope, which permits MRI to study small sample sizes ($<$ $2mm$) at high resolution (up to $2\mu m$).

The effects of molecular diffusion and local variations in the magnetic susceptibility in NMR microscopy are described, which, along with the intrinsic low sensitivity of NMR, are the fundamental limitations to resolution. Molecular diffusion in the presence of a magnetization grating not only broadens the point spread function but also reduces the signal intensity. The significance of these effects depends strongly on the magnetic field gradient strengths and imaging protocols. A NMR microscope for a standard bore $14.1T$ magnet was developed, it is equipped with a highly efficient solenoidal RF coil and three orthogonal gradients with strengths of $1260G/cm$ for G_z, $760G/cm$ for G_y, and $410G/cm$ for G_x at 15A. A modified CTI sequence is presented which incorporates strong pulsed gradients, Ernst angle excitation, CP coherent detection and reduced k-space sampling. It is the optimal pulse sequence for acquiring high-resolution ($< 5\mu m$) NMR images (best signal-to-noise ratio per unit time) when the effect of molecular diffusion is significant. It is demonstrated that this new sequence makes it possible to acquire images with a high resolution of $2\mu m \times 2\mu m \times 8\mu m$ within a few hours.

A wide variety of images have been acquired using the new microscope, and representative images are presented to demonstrate the potential of NMR microscopy as a new tool in developmental biology research. In particular, used in combination with other biological techniques, NMR microscopy can provide a robust, non-invasive, 3D imaging approach to quantifying changes in structure due for instance to radiative exposure, therapy, and natural growth or genetic modifications.

Thesis Supervisor: David G. Cory
Title: Associate Professor

Acknowledgments

My graduate years at MIT have been filled with good times during which I learned and grew intellectually and personally. It is with great pleasure that I acknowledge the many people that make this experience possible and enjoyable.

I would like to especially thank my thesis supervisor, Prof. David G. Cory who, more than anyone else, is responsible for the fulfillment of this work. His invaluable steering advice and abundant ideas always kept the research focused in the right direction. His kindness and encouragement have made my thesis work a most delightful and memorable experience.

My gratitude is due to my thesis reader, Prof. Sow-Hsin Chen, for his constant interest and encouragement. My sincere gratitude is also due to Dr. Werner E. Maas for his generous help and warm friendship. Many thanks go to my colleagues for always willing to help and making the lab a pleasant and productive place. And I am grateful to Julie Agapite, Jay Murthy, and Alan Jasanoff for providing me with biological samples.

My very special thanks go to my grandparents, parents, and sisters. Their unconditional love has always been the greatest inspiration in my life. I can not thank them enough for their support, understanding and patience.

Finally, love and thanks to my husband, Xuefeng Cheng.

This thesis is dedicated to my beloved family.

Contents

List of Figures

List of Tables

Chapter 1

Background

1.1 Introduction

Nuclear Magnetic Resonance (NMR) microscopy is an extension of nuclear magnetic resonance imaging (MRI) with resolution approaching a few microns. It has been shown to have promise in both biology [1] and medicine [25] ever since mid-1980's. Compared to other microscopy techniques, NMR microscopy has two advantages: first, it allows nondestructive investigation of three dimensional information; second, it has multiple contrast mechanisms based on parameters such as spin density, relaxation times, molecular diffusion, flow, and metabolism. It is one of the most promising approaches to determining the spatial distribution and dynamic changes of small features in biological samples.

NMR microscopy has much in common with its medical counterpart MRI. However, the instrumentation and resolution limits for microscopy are quite different and the potential applications of NMR microscopy are largely unexplored. In part, the delay in the expanded use of NMR microscopy is tied to a lack of commercial development of the necessary NMR transducers, and to the necessity of employing high-field magnets, but applications have also been limited by the rather modest spatial resolution normally achieved. Here the limited resolution has been addressed by designing and building NMR microscopes based on a 600MHz standard-bore magnet, and developing a series of efficient protocols for obtaining high resolution images.

The instrumentation and methods developed are presented along with the reasons behind the choices that were made in developing the systems. Representative images are shown in chapter 5 to demonstrate the potential of NMR microscopy in various research areas. Chapter 6 closes with a discussion of future work and a view of the future roles of NMR microscopy.

1.2 Elementary Description of NMR

Among the various atomic nuclei, about a hundred isotopes possess an intrinsic angular momentum, called spin and written $\hbar \vec{I}$. They also possess a magnetic moment $\vec{\mu}$ that is proportional to their angular momentum:

$$\vec{\mu} = \gamma \hbar \vec{I}. \tag{1.1}$$

The coefficient γ, characteristic of each nuclear species, is called gyromagnetic ratio, and $\hbar$ is Planck's constant divided by 2π. The energy of a magnetic moment $\vec{\mu}$ in a magnetic field $\vec{B}_0$ is equal to:

$$E = -\vec{\mu} \cdot \vec{B}_0. \tag{1.2}$$

In quantum mechanics, the magnetic moment of a nuclear spin is an operator $\hat{\mu}$ proportional to the spin operator $\hat{I}$. To the classical energy (1.2) there corresponds a quantum mechanical Hamiltonian operator called the Zeeman Hamiltonian:

$$\hbar \mathcal{H} = -\gamma \hbar B_0 \hat{I}_z, \tag{1.3}$$

given that the magnetic field is along the direction z. The spin operator $\hat{I}_z$ is quantized: its possible values $I_z = m$ vary in steps of one unit from $-I$ to I. To each value of m there corresponds a quantum level of energy:

$$E_m = -\gamma \hbar B_0 m. \tag{1.4}$$

For spins with $I = 1/2$, such as H^1 (proton), and F^{19}, there are two energy levels: $E_- = \gamma\hbar B_0/2$, when the spins are antiparallel to the static magnetic field $\vec{B_0}$, and $E_+ = -\gamma\hbar B_0/2$, when the spins are parallel to the static field. The majority of imaging experiments are measurements of the proton spin densities since H^1 has the highest gyromagnetic ratio among all stable nuclei and are nearly 100% naturally abundant as well as being the main constituent of many materials.

In order to observe an NMR signal, transitions between two different energy levels must be induced. For this purpose, in addition to the large steady field $\vec{B_0}$, a small Radio-Frequency (RF) field $\vec{B_1}$ normal to $\vec{B_0}$ and of frequency ω (on the order of $100MHz$) is applied. The Zeeman interaction of the nuclear magnetic moments with the RF field then connects the two energy levels (for spin 1/2) under the condition that ω equals to the resonance frequency $\omega_0 = -\gamma B_0$, so called Larmor frequency.

Although NMR is a quantum mechanical phenomenon, the bulk magnetic moment $\vec{M}$ for an assembly of a large number of identical spins with $I = 1/2$ can be considered as classical vectors. The Larmor theorem states that the motion of the magnetic moment $\vec{M}$ in a magnetic field $\vec{B_0}$ is a precession around that field, and can be described by:

$$\frac{d\vec{M}}{dt} = \gamma\vec{M} \times \vec{B_0}. \tag{1.5}$$

However, this equation is correct only for isolated magnetic moments. In fact the atoms and their nuclei are usually embedded in a medium of condensed matter, liquid or solid, and the nuclear magnetic moments are coupled to the other degrees of freedom of that medium, traditionally called 'the lattice'. This coupling, called the spin-lattice coupling, tends to produce an evolution towards the common thermal equilibrium between the spin system and the lattice. So starting from a state out of equilibrium, the dynamics of the bulk magnetization is composed of two kinds of motion, precession about the external magnetic field as described in Eq 1.5, and relaxation back to the equilibrium state exponentially, but with two different time constants: T_1 (spin-lattice relaxation time) for the longitudinal component and T_2 (spin-spin relaxation time) for the transverse components. By adding the relaxation

terms to Eq 1.5, one obtains the Bloch equations:

$$\frac{d\vec{M}}{dt} = \gamma \vec{M} \times \vec{B_0} - \frac{1}{T_1}(M_z - M_0)\vec{k} - \frac{1}{T_2}(M_x\vec{i} + M_y\vec{j}), \qquad (1.6)$$

where $\vec{i}$, $\vec{j}$ and $\vec{k}$ are unit vectors in the directions x, y and z respectively. At thermal equilibrium, the energy levels $(\pm\gamma\hbar B_0/2)$ are occupied by a collection of spins according to the Boltzman distribution. In a static magnetic field strength of $14.1T$, the population difference is about 1 spin in 10^4,

$$\frac{N_-}{N_+} = e^{-\gamma\hbar B_0/k_B T}, \qquad (1.7)$$

where k_B is the Boltzman constant, N_- and N_+ are the numbers of spins anti-parallel and parallel to the static magnetic field. The longitudinal magnetization M_z at thermal equilibrium, which is along the direction of $\vec{B_0}$, has a non-vanishing value M_0, whereas the transverse components M_x and M_y vanish:

$$M_0 = \mu(N_- - N_+), M_x = 0, M_y = 0. \qquad (1.8)$$

Since M_0, the detectable net magnetization, is so small, NMR experiments are relatively insensitive and normally greater than 10^{13} spins are required for detection.

The NMR signal is measured by a tuned RF coil coupled to the sample. A RF pulse is applied through the coil to excite the spin system, which brings the system away from thermal equilibrium. Then the bulk magnetization is allowed to precess and relax freely. The transverse components of the bulk magnetization rotating about the z-axis induce an e.m.f. in the RF coil by Faraday's law and the induced e.m.f. is collected after being mixed with the output from a reference RF oscillator, a process known as heterodyning. This is equivalent to observe the magnetization in a rotating frame, where Bloch equations can be written explicitly as:

$$\frac{dM_x}{dt} = \Delta\omega M_y - \frac{M_x}{T_2}$$

16

$$\frac{dM_y}{dt} = -\Delta\omega M_x - \frac{M_y}{T_2}$$
$$\frac{dM_z}{dt} = \frac{M_0 - M_z}{T_1}, \tag{1.9}$$

where $\Delta\omega$ is the small offset between the rotating frame frequency and the Larmor frequency. The transverse magnetization as a function of time can be easily solved from Eq 1.9,

$$M_+(t) = M_0 e^{-i\Delta\omega t} e^{-t/T_2}, \tag{1.10}$$

where $M_+(t) = M_x(t) + iM_y(t)$, the complex notation of transverse components. After the heterodyning process, the measured signal has the form,

$$S(t) = S_0 e^{i\phi} e^{-i\Delta\omega t} e^{-t/T_2}, \tag{1.11}$$

where ϕ is the receiver phase and S_0 is the signal amplitude immediately after the RF pulse, a number which is simply proportional to M_0. As shown in Eq 1.11, the NMR signal is measured in the time domain as an oscillating, decaying e.m.f. induced by the transverse magnetization during free precession. It is therefore called the Free Induction Decay(FID). By Fourier transformation the same signal may be represented in the frequency domain. This process is shown in Fig. 1-1 for the case $\phi = 0$. The result in the real part of the domain is a Lorentzian line-shape of cyclic frequency offset $\Delta\omega/2\pi$ and Full-Width-Half-Maximum (FWHM) $1/\pi T_2$, the so-called absorption spectrum. The imaginary line-shape is known as the dispersion spectrum and for this function the width is somewhat greater.

1.3 Introductory Spin Manipulation

Among the enormous number of pulse sequences which are used in modern NMR, there are a few whose origins date from the birth of the subject but whose usefulness makes them fundamental for generating new pulse sequences. These are the inverse recovery, spin echo, CPMG echo train, stimulated echo, etc. Each is concerned with
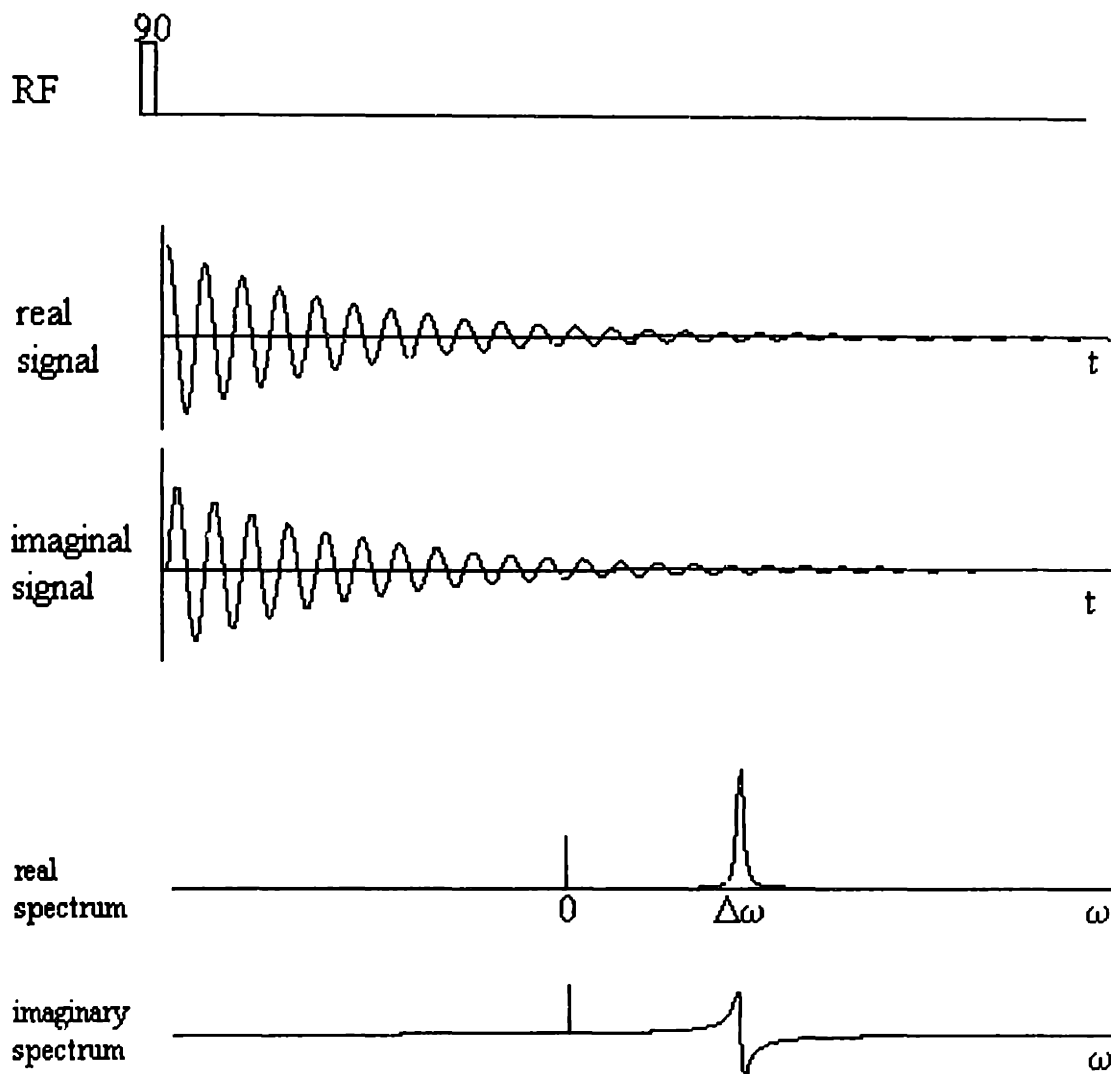
Figure 1-1: Free Induction Decay (FID) following a single 90° RF pulse. The real and imaginary parts of the signal correspond to the in-phase and quadrature receiver outputs. The signal is depicted with receiver phase $\phi = 0$ and, on complex Fourier transformation, gives real absorption and imaginary dispersion spectra at the offset frequency, $\Delta\omega = \omega_0 - \omega$.

the manipulation of the spin system under the influence of the Zeeman Hamiltonian and the T_1 and T_2 relaxation processes, and each can be understood using the semi-classic description of NMR. The following are some of the basic elements of the optimal imaging pulse sequence developed in this theis work for high resolution MRI.

Signal Averaging

The oscillating e.m.f. induced in a receiver coil by precessing magnetization is superposed on the noise e.m.f. arising from random thermal motion of electrons in the receiver coil wire and the comparative size of the signal and noise e.m.f.s is known as the signal-to-noise ratio(SNR). Because of the low sensitivity of NMR, it is customary to co-add signals from N successive experiments in order to enhance the SNR. Successive addition has the effect that the signals add coherently while the noise adds in random phase. Because the noise power is additive, the r.m.s. noise amplitude is proportional to $\sqrt{N}$. As a result, the SNR improves as $N/\sqrt{N}$ or $\sqrt{N}$.

Phase Cycling

Since the phase of NMR signal depends on the excitation pulse phase, it becomes possible to distinguish the desired signal from any background interference or error by a succesive alternation of r.f. transmitter and reveiver phases. Phase cycles enable a experimentalist to correct for phase and amplitude anomalies in quadrature detection (QD), transverse magnetization interference due to rapid pulse repetition, and echo artefacts due to pulse amplitude errors, which are the primary causes of artefacts in NMR imaging. A four-pulse CYCLOPS [23] and EXERCYCLE [52] can nicely correct the phase and amplitude errors in QD and echo artefacts respectively. These two phase cycles are so useful that they are generally incorporated as subcycles of all other phase cycles.

Spin Echo

Magnetic field inhomogeneity (ΔB_0) causes nuclear spins to precess at differing Larmor frequencies according to their location in the sample. This spread of Larmor

frequency causes a dephasing of transverse magnetization following a 90° RF pulse. Trasverse magnetization phase coherence therefore lasts only for a time of order $(\gamma \Delta B_0)^{-1}$, a transience which apparently constrains the length of time over which this magnetization can be manipulated or detected. Many years ago E. Hahn [21] recognized that this loss of phase coherence was inherently reversible. Application of a second 180° RF pulse after a time delay τ will cause refocusing at 2τ as shown in figure 1-2. The spin echo sequence refocuses all dephasing due to inhomogeneous broadening, chemical shift, and heteronuclear J-coupling.
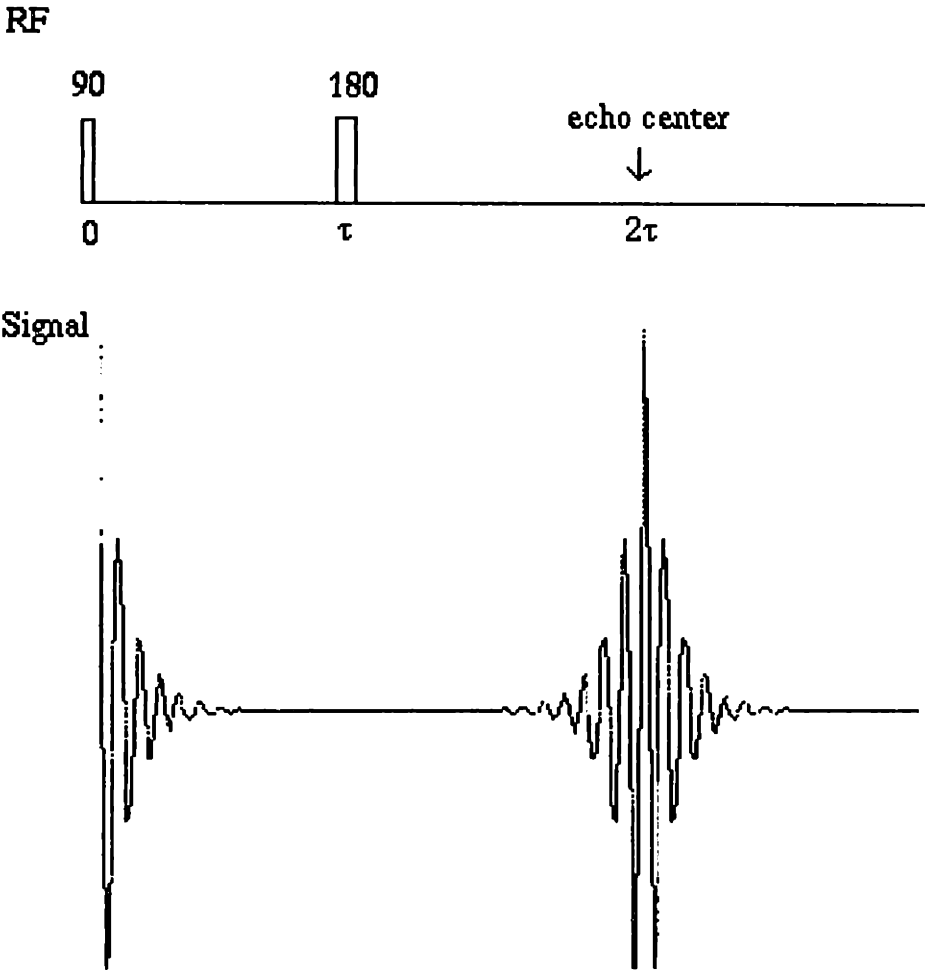
Figure 1-2: Spin echo pulse sequence and signal.

1.4 Principles of NMR Imaging

1.4.1 Reciprocal Space and Fourier Transformation

In NMR spectroscopy, the spectrum of nuclear precession frequencies (ω) gives information about the chemical environment of the spins and it is important to arrange that the static magnetic field, B_0, vary as little as possible across the sample. By contrast, a linearly varying field, known as a field gradient, is applied on purpose in NMR imaging. In the presence of a magnetic field gradient $\vec{G}$, the local Larmor frequency is

$$\omega(\vec{r}) = \gamma B_0 + \gamma \vec{G} \cdot \vec{r}, \tag{1.12}$$

where

$$\vec{G} = \frac{\partial B_z}{\partial x}\hat{x} + \frac{\partial B_z}{\partial y}\hat{y} + \frac{\partial B_z}{\partial z}\hat{z}. \tag{1.13}$$

This simple linear relation between the Larmor frequency and the nuclear spin coordinates, $\vec{r}$, lies at the heart of MRI imaging. The evolution of spins in a linear magnetic field gradient creates a periodic phase modulation of the local spin magnetization that may be described as a magnetization grating. The observed NMR signal is the bulk magnetization integrated over the sample, derived from Eq 1.10,

$$M_+(t) = M_0 e^{-t/T_2} \int \rho(x, y, z) e^{-i\gamma \vec{G} \cdot \vec{r} t} dx\,dy\,dz, \tag{1.14}$$

where $M_0 \rho(x, y, z)$ is the spatial distribution of spin magnetization. Eq 1.14 takes a more recognizable form by introducing the reciprocal space vector $\vec{k}$,

$$k_x = \gamma \frac{\partial B_z}{\partial x} t, \;\; k_y = \gamma \frac{\partial B_z}{\partial y} t, \;\; k_z = \gamma \frac{\partial B_z}{\partial z} t. \tag{1.15}$$

So that

$$M_+(t, \vec{k}) = M_0 e^{-t/T_2} \int \rho(x, y, z) e^{-ik_x x} e^{-ik_y y} e^{-ik_z z} dx\,dy\,dz, \tag{1.16}$$

where $M_+(t, 0)$ is the signal in the absence of the magnetic field gradient. From this equation, we can see that NMR images are recorded as a set of Fourier components of

the sample's spin density, $\rho(x, y, z)$, obtained through the spatially varying precession rates of spins in a magnetic field gradient [34, 6, 31]. The magnetization grating serves the purpose of selecting which Fourier component of the spin density is observed. The NMR signal in the presence of a magnetic field gradient is the Fourier transform of the spin density convoluted with the NMR line-shape in the absence of the gradient. Once a complete set of the sample's spatial Fourier components is recorded, the image may be reconstructed by a Fourier transformation, in which case the natural NMR line-shape acts to limit the spatial resolution,

$$Image = Spin\,density \otimes NMR\,line\,shape + Noise. \qquad (1.17)$$

The above convolution makes sense only when the frequency axis of the NMR line shape is rescaled to spatial units: In a time-independent magnetic field gradient, the frequency axis may be rescaled through the proportionality constant,

$$\frac{\gamma}{2\pi} \frac{\partial B_z}{\partial r}. \qquad (1.18)$$

Eq 1.17 underscores the inherent simplicity of the NMR imaging experiment, which is ideally linear and with a spatially invariant resolution. To this point, the only restriction on the spatial resolution is that given by the Nyquist condition,

$$\Delta x = \frac{\pi}{k_{max}}. \qquad (1.19)$$

Therefore, a certain range of k-space must be scanned in order to achieve an NMR image with a desired resolution.

Frequency Encoding and Phase Encoding

We can scan the k-space by either a frequency encoding or a phase encoding method, which are illustrated in Fig. 1-3 for the 1D case. As shown in Eq 1.15, the direction and magnitude of k-vector depend on the direction and strength of the magnetic field gradients, and the duration of the gradient pulse. In the frequency encoding method,

data are collected while the gradient is on. Since the k value changes continuously during data collection, the collected data correspond to sequential k components in the reciprocal space. By this method, k-space is traversed parallel to the direction of the field gradient in a single excitation. In the phase encoding method, a single k component is collected following each excitation after the gradient is off and this process is repeated with incrementing either the gradient strength or the gradient on-time while other conditions are kept unchanged. Although both methods are essentially the same in a sense that in either way we can traverse k-space, their effects on the imaging experimental time and the image quality are quite different. It requires N excitations to collect N data points in k-space by phase encoding method while the same information can be achieved in a single excitation by frequency encoding. Hence, phase encoding is much more time consuming. However, image distortions due to time-independent internal Hamiltonians show up in the frequency encoding detection but not in the phase encoding detection. Another difference, which is the most important factor in high resolution NMR imaging, is found in the relative signal attenuation due to molecular diffusion. This will be extensively discussed in chapter 2.

1.4.2 Resolution and Distortions

To the extent that the actual measurement follows the linear model in Eq 1.17, each contributor to the system's resolution (or point spread function) may be identified and explored independently. However, there are also nonlinear contributors that introduce image distortions. The resolution limit provides a length scale below which one should not attempt to extract spatial information, but distortions may easily impair the image quality on any length scale. For this reason, special care is usually taken to design the imaging method so as to limit distortions.

As described above, the NMR signal is a measure of the Fourier components of the spin density. A equivalent real space picture is that spin evolution in the presence of a magnetic field gradient introduces a magnetization grating (a linear phase ramp) across the sample as shown in Fig. 1-4. The k-vector describes the periodicity of this

grating,

$$k_i = 2\pi/\lambda_i, \ i = x, y, z, \tag{1.20}$$

where λ is the period of the grating. To obtain high-resolution requires that a fine gating be prepared without loss of the grating's amplitude, and to avoid distortions requires that the spatial modulation of the magnetization be correctly described in terms of a single wave number.

Linewidth Contributions

Since the grating is created via the differential rate of spin evolution introduced by the magnetic field gradient, there is a practical limit on the rate at which a grating may be created. Naturally, then there is a competition between the time to develop the grating and the T_2 decay of the transverse magnetization, which in turn limits the spatial resolution to,

$$\Delta r = \frac{2}{\gamma \frac{\partial B_z}{\partial r} T_2}. \tag{1.21}$$

This is equivalent to treating the line-width $\nu_{1/2} = 1/\pi T_2$ as a Lorentzian convolution Point-Spread-Function (PSF).

The resolution limit introduced by the spin-spin relaxation is spatially uniform for a given type of spin. Fortunately, this limit is not usually severe, since gradients of greater than a few hundred Gauss per centimeter are easily made, and spin-spin relaxation times are typically much longer than the fraction of a millisecond required to burn the grating. Since the gradient interaction is secular, a constant time encoding experiment maps the PSF into an attenuated delta function and the resolution is correspondingly increased at the cost of some sensitivity.

Notice that T_2^* is not important in this discussion, since the resolution is limited only by the line-width over a voxel, and not that integrated over the sample. However, for sensitivity purposes, it is often best to employ spin echoes to refocus T_2^* losses (see section 1.3).

24

Molecular Diffusion

It is widely accepted that the single most important factor limiting resolution in NMR microscopy is molecular diffusion [36, 10, 9, 24]. Since the diffusion constant of free water is approximately $2.5\mu m^2/ms$ and with even strong gradients a few milliseconds are required to create a grating with a pitch of $1\mu m$, molecular diffusion will tend to blur the magnetization grating. The influence of molecular motions on a magnetization grating is describable through the conditional probability of spin (or molecular displacements, $P(\vec{r}|\vec{r}',t)$, the probability that a spin initially at r will be at r' at a time t). The well known attenuation behavior of molecular diffusion in a grating is associated with a uniform sample of infinite spatial extent, where the normalized probability of molecular displacement is strictly Gaussian,

$$P_{diff} = \frac{1}{2\sqrt{\pi Dt}}exp(-\frac{x^2}{4Dt}), \qquad (1.22)$$

with D being the molecular diffusion constant.

Molecular diffusion in a constant grating modifies the grating as a convolution with the spread of the molecules,

$$exp(-i\vec{k}\cdot\vec{r}) \otimes P_{diff}. \qquad (1.23)$$

Employing the Weiner-Kintchine theorem of Fourier convolution, the attenuation of the magnetization grating by diffusion over a time t is

$$exp(-k^2 Dt). \qquad (1.24)$$

A lovely part of the solution is that for this geometry, molecular diffusion does not change the pitch of the grating; it is solely an attenuation. So molecular diffusion (provided that it is Gaussian) may limit the resolution of the image, but it does not introduce new Fourier components, and consequently will not distort the image. Details concerning signal loss and PSF broadening introduced by molecular diffusion are discussed in chapter 2 & 3.

Magnetic Susceptibility

In heterogeneous samples, it is expected that the magnetic susceptibility will be spatially varying, and thus the magnetic field variations will not arise solely from the applied gradients. This leads to image distortions, since now the magnetization grating will no longer have a uniform pitch throughout the sample. A common pronounced example of this is seen in samples with air pockets. Static susceptibility variations and the line broadening associated with these can be refocused, and are hence avoidable by spin echoes. However, there is a second more subtle influence of susceptibility. Due to molecular diffusion in the background gradients, the ability to refocus is limited. The resulted signal attenuation in spin echo contributes to both PSF broadening and sensitivity loss. In order to reduce this attenuation, strong gradients and short echo time are preferable. The applied gradients should greatly dominate any gradients introduced by susceptibility variations.

Sensitivity

The achievable resolution not only depends on the width of the PSF, but is also limited by noise, an important component of the linear model (Eq 1.17). Without noise, the PSF can be deconvoluted from the image and the resolution is solely limited by sampling. Unfortunately, NMR is very insensitive. The NMR signal, oscillating e.m.f. induced in an RF coil by the precessing nuclear spin magnetization, is superimposed on the noise e.m.f. arising from the random thermal motion of electrons in the RF coil and preamplifier and the magnetically induced eddy current in the sample. The comparative size of the signal and noise e.m.f.'s is known as the signal-to-noise ratio (SNR). The SNR provides a fundamental limitation to resolution in magnetic resonance microscopy since the signal available from each volume element decreases as the voxel size is reduced [8]. Without reference to specific imaging techniques, Mansfield and Morris [35] have shown by a simple argument that the acquisition time

for a sample of volume $(\Delta x)^3$ is given by

$$t = (\frac{\rho_0}{\sigma_f})^2 a^2 (\frac{T_1}{T_2}) \frac{2.8 \times 10^{-15}}{f^{7/2}} (\frac{1}{\Delta x})^6 \qquad (1.25)$$

Where (ρ_0/σ_f) is the desired proton NMR SNR, a is the RF coil radius, and f the spectrometer frequency in MHz. This implied the dependence of the imaging co-addition time on the sixth power of the resolution. It is expected that the sensitivity limit acts as a sort of 'brick wall' which stands in the way of further improvements in resolving power by the method of signal averaging. In another word, instrumentation and methodology developments are essential to further resolution improvements in NMR imaging.

RF

n data points

one point

Gradient

Repeat
n times

(a)

(b)

Scanning k-space

k_1 k_2 . . . k_n
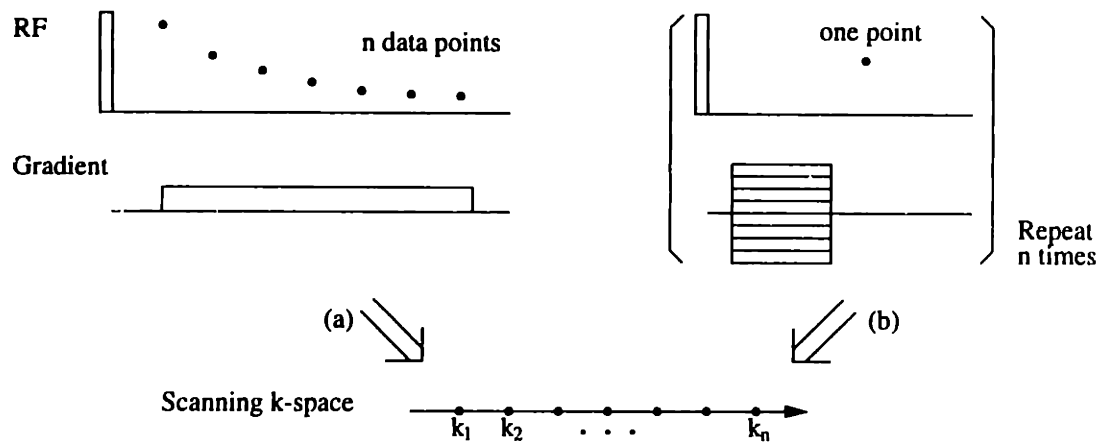
Figure 1-3: Frequency encoding and phase encoding in 1D imaging. (a)In the case of frequency encoding, a series of k-components is collected after a single excitation while the gradient is on. (b) In phase encoding, one k-component is collected at a time after the gradient is turned off. The gradient on time or strength is changed systematically to traverse the k-space.

$\lambda = 1/k$
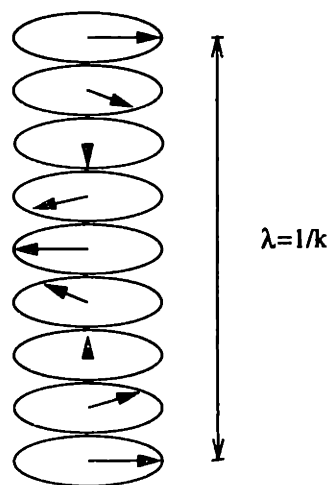
Figure 1-4: Magnetization grating induced by spatially dependent phase evolution of spins under magnetic field gradient.

Chapter 2

Effects of Molecular Diffusion

Molecular diffusion is inevitable in liquid state NMR imaging experiments. In the presence of a magnetic field gradient, it leads to random fluctuations in Larmor frequency and thus an irreversible phase decoherence of the spins. While the effects of molecular diffusion on images can be subtle, as a "rule of thumb" the parameter of significance is $\Delta x_{diff}/\Delta x_{pixel}$, where Δx_{diff} is the r.m.s. displacement of the spins over the signal-acquisition period and Δx_{pixel} is the pixel dimension. Given that acquisition periods are usually on the order of several milliseconds, Δx_{diff} is on the order of $10\mu m$. Therefore, the effects of molecular diffusion are extremely important in NMR microscopy [6, 2, 11]. It not only broadens the point spread function but also reduces the signal intensity. In some cases, molecular diffusion causes a fundamental limitation to the resolution, which dominates the intrinsic sensitivity limit. However, $\Delta x_{diff}/\Delta x_{pixel}$ only measures the overall significance of diffusion in NMR imaging, its precise effect depends strongly on the sample property and the imaging pulse sequence employed.

2.1 Free Diffusion

2.1.1 Diffusive Attenuation in Frequency Encoding and Phase Encoding

Using Torrey's equation [48] or a random walk model [6], it is rather simple to calculate the signal attenuation due to free diffusion. This has been investigated by Cho [2] and Callaghan [9, 8]. Here diffusion limited resolutions are calculated for frequency encoding (FE) and phase encoding (PE) directions with spin echoes (Fig. 2-1).
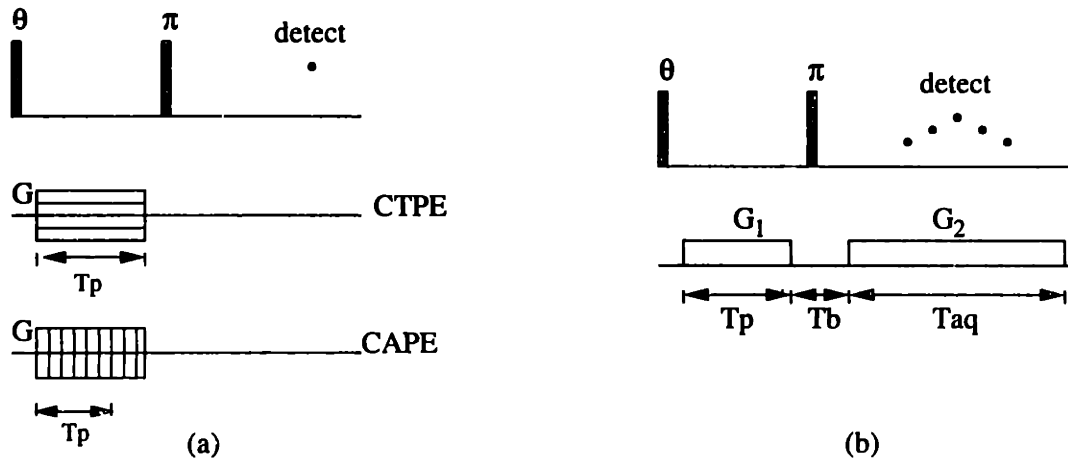
Figure 2-1: Pure phase-encoding (a) and frequency-encoding (b) spin echo pulse sequences.

For pure phase encoding with uniform orthogonal gradient pulses of duration T_p, i.e. constant time phase encoding (CTPE), the signal loss due to diffusion is,

$$A_p(k) = exp(-k^2 DT_p/3). \tag{2.1}$$

To minimize the diffusive signal attenuation, a constant amplitude phase encoding

(CAPE) method can be used, where

$$A_p(k) = exp(-\frac{|k|^3 D}{3\gamma G}),$$ (2.2)

G is the maximum gradient strength available. In both cases, the attenuation function is symmetric in k-space and equals to one at $k = 0$. Therefore, free diffusion introduces no distortion or intensity loss to the reconstructed image along the phase-encoding directions. Instead, it contributes to the overall PSF which leads to blurring of sharp features in the image. This blurring effect can be greatly reduced with strong gradients and proportionally shorter phase encoding time.

With frequency encoding (FE), the situation is a little more complicate. The diffusive attenuation is given by,

$$A_f(k) = \underbrace{exp[-\frac{Dk_m^3}{3\gamma G_1}] \cdot exp[-k_m^2 DT_b] \cdot exp[-\frac{Dk_m^3}{3\gamma G_2}]}_{A_f(0)} \cdot exp[-\frac{Dk^3}{3\gamma G_2}],$$ (2.3)

where $k_m = \frac{\pi}{\Delta x}$, and G_1, G_2, T_b are the phase-encoding gradient, readout gradient and the time delay between them (Fig. 2-1b). The first part, $A_f(0)$, causes an overall image attenuation, while the second part causes a broadening of PSF only. Fig. 2-2 shows $A_f(0)$ as a function of resolution in spin echo imaging (SEI) experiments. With FE, molecular diffusion reduces signal intensity significantly, which is a much more drastic effect than the blurring of images. Unfortunately, this attenuation action can not be suppressed by simply employing strong gradients. The read gradient G_2 is usually limited by receiver bandwidth and the thermal noise increases as the square root of G_2. As shown in Fig. 2-3, 90% of the signal is lost for $2\mu m$ resolution if the diffusion coefficient is $2\mu m^2/ms$. Therefore, it is practically impossible to acquire high resolution ($< 5\mu m$) images with SEI unless the rate of molecular diffusion is quite slow. In chapter 3, constant time imaging (CTI) sequence will be introduced, where pure phase encoding is used along all spatial directions. With CTI, it is possible to reach the resolution limit of $2\mu m$ as shown in Fig. 2-4. The diffusion limited resolution depends strongly on the gradient strength and the molecular diffusion

rate. With a strong gradient, $1000G/cm$, the highest resolution possible for free water ($D = 2\mu m^2/ms$) is around $2\mu m$. For molecules diffuse an order of magnitude slower ($D = 0.1\mu m^2/ms$, the typical diffusion coefficient of intra-cellular water[4]), it is down to $1\mu m$. This number is too optimistic, however, for two reasons. First, not only diffusive broadening but also available signal intensity sets the resolution limit. Second, in heterogeneous environments, where local gradients exist, diffusive signal attenuation is more pronounced.
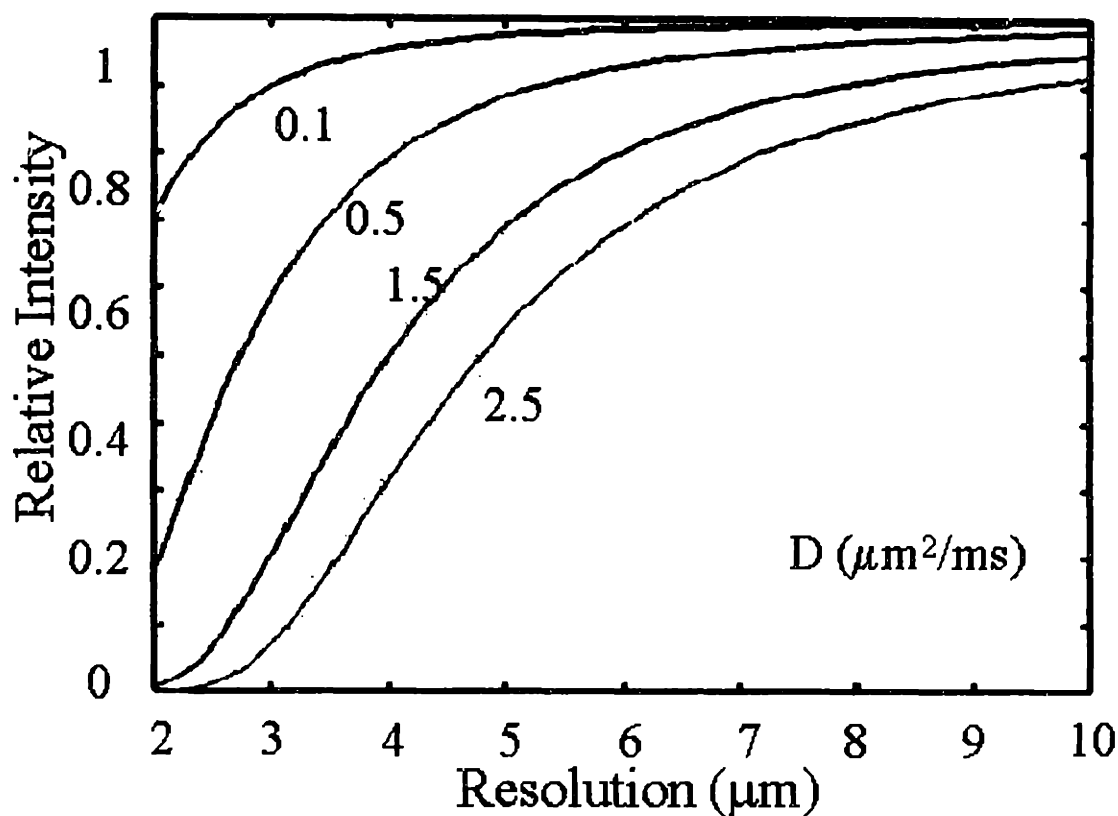
Figure 2-2: Relative signal intensity (with vs. w/o molecular diffusion) in spin echo imaging experiments as a function of resolution. At high resolutions ($< 5\mu m$), SEI is only useful for imaging samples with very slow molecular diffusion. The maximum gradient strength is assumed to be $300G/cm$.
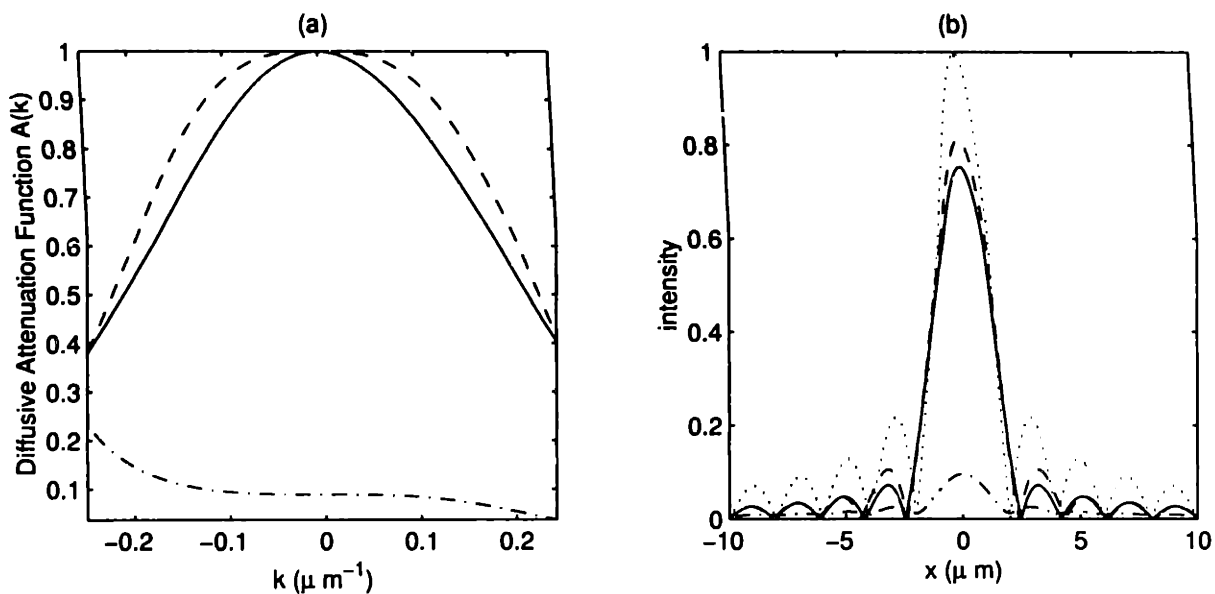
Figure 2-3: Diffusive attenuation functions in k-space (a) and their correspondent
PSF's (b). In this calculation, the diffusion constant is assumed to be $2\mu m^2/ms$,
and the maximum gradient strength is $1000G/cm$. The k-space attenuation is sym-
metric and there is no intensity loss in both cases of constant time (solid line) and
constant amplitude (dashed line) phase encoding. The k-space attenuation for fre-
quency encoding (dash dotted line) is much more severe, but flatter. The dotted line
indicates the PSF when there is no molecular diffusion. It has a $FWHM$ of $2\mu m$,
which is the resolution resulting from k-space truncation.
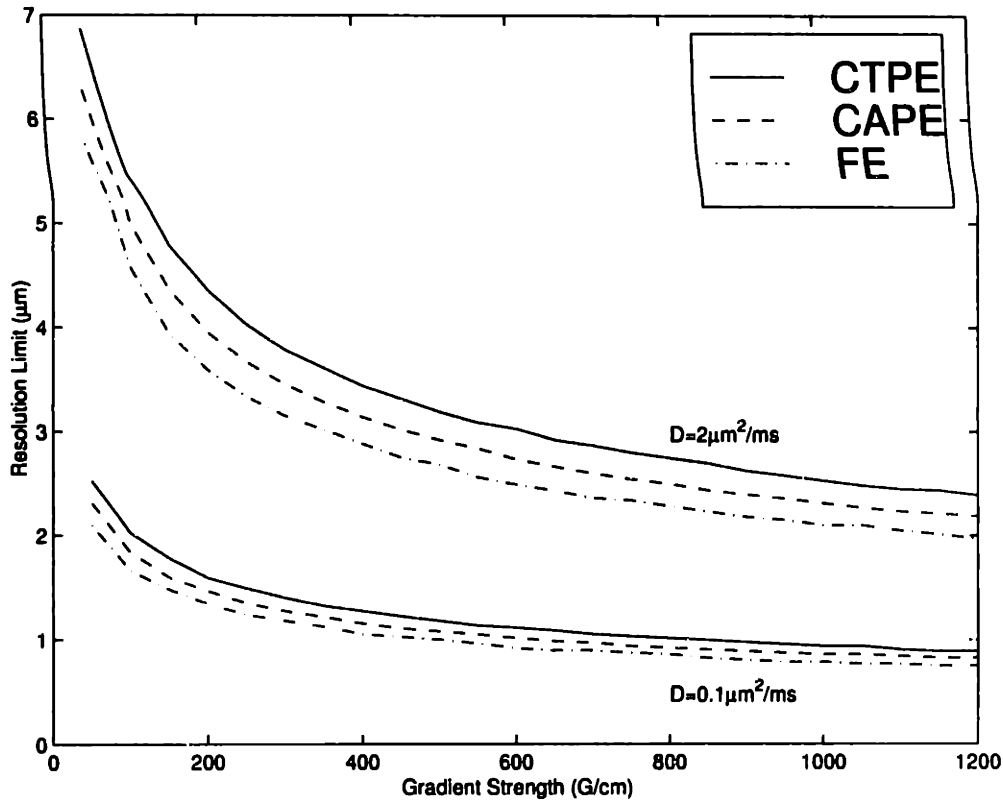
Figure 2-4: Diffusion limited resolution as a function of maximum gradient strength.

2.1.2 Diffusive Attenuation During Slice Selection

The signal attenuation during slice selection increases remarkably as the slice thickness decreases [12]. A typical slice selection sequence is shown in Fig. 2-5. If a two cycle sinc function is used for the soft pulse and the pulse duration is 2τ, the signal attenuation factor can be expressed in terms of the slice thickness Δz,

$$A = exp(-\frac{32\pi^2 D\tau}{3\Delta z^2}) = exp(-\frac{128\pi^3 D}{3\gamma G\Delta z^3}), \tag{2.4}$$

where G is the gradient strength. G and τ are correlated through the excitation bandwidth Δf,

$$\Delta f = \frac{2}{\tau} = \frac{1}{2\pi}\gamma G\Delta z. \tag{2.5}$$

Figure 2-6 shows the diffusive signal attenuation as a function of gradient strength and slice thickness. Here, the diffusion constant is assumed to be $2\mu m^2/ms$. With

34

strong gradient and short RF pulse, the signal attenuation will be suppressed. The slice thickness in Fig. 2-6(a) is $40\mu m$, which is about the thinnest slice achievable without significant signal loss, as shown in Fig. 2-6(b). A relatively thick slice ($> 40\mu m$) is usually selected for further three dimensional imaging if even higher resolution is desired along the slice direction.
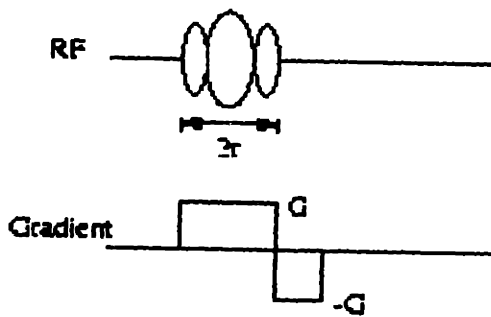
Figure 2-5: Slice selection with a soft RF pulse and magnetic field gradient.
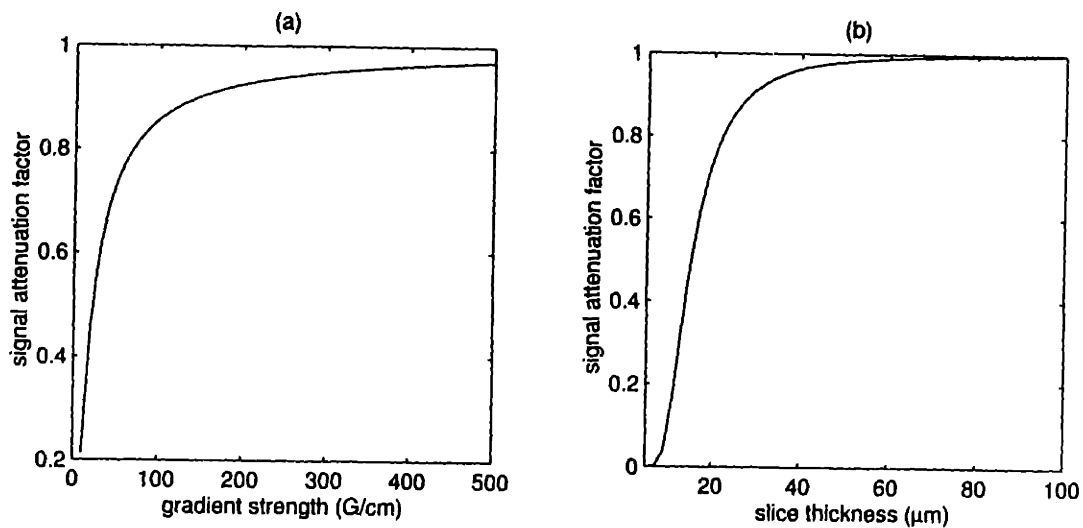
Figure 2-6: Diffusive signal attenuation as a function of gradient strength (a) and slice thickness (b). A gradient strength of $410G/cm$ is assumed in (b).

2.2 Diffusion in Heterogeneous Samples

The study of heterogeneous samples (e.g. emulsion, biological and geologic specimens) by NMR presents unique challenges, because the sample itself introduces modulated local diffusion coefficients or magnetic fields. Therefore, the assumption that both D and G are uniform is somewhat unrealistic. Examples are restricted diffusion [24, 7] and free diffusion in the presence of susceptibility induced background gradients.

2.2.1 Correlated Susceptibility and Diffusion Effects

Variations in the isotropic bulk magnetic susceptibility, which introduce spatially varying local fields, are a fundamental complication of NMR studies of spatially heterogeneous samples. The influence of these local fields on the NMR signal depends on both the strength of the local magnetic field gradient and on the rate at which the molecules diffuse through the gradient. Three motional regimes may be distinguished based on the homogeneous T_2, the inhomogeneous T_2, and attenuation in an echo experiment:

static case there is a resolvable frequency shift and hence an extra inhomogeneous linebroadening, but the homogeneous T_2 remains unchanged and the attenuation under an echo train consistently measures this.

slow motion there is still a resolvable frequency shift and an extra inhomogeneous linebroadening. The echo attenuation as measured via a Carr-Purcell train depends upon the pulse spacing. Both T_2 and D measurements via echo and pulsed gradient echo sequences are compromised by the presence of the background gradients.

fast motion the molecular motions themselves blur the differences between spatial locations and the homogeneous T_2 is reduced.

In the static case, the artifacts caused by susceptibility in NMR microscopy are well documented [40, 9, 6]. Along the frequency encoding direction, each element of the object is displaced from the original position $\vec{r}$ to $\vec{r} + \Delta B_0(\vec{r})/G_r$, where $\Delta B_0(\vec{r})$

36

and G_r are the local field and read gradient. In order to avoid image distortion, G_r should be high enough that the applied gradient field across a single pixel dominates the local-field offset. However, a price is paid in sensitivity by increasing the receiver bandwidth. On the other hand, pure phase encoding introduces no element displacement but may lead to image phase distortions. Phase distortion is not a concern unless phase mapping is desirable or significant phase variation occurs across one pixel. The latter will lead to local signal attenuation. Fortunately, phase distortion can be easily removed by using spin echoes.

In NMR microscopy, molecular diffusion in the presence of susceptibility inhomogeneity generally falls in the slow motion regime. There are two effects associated with it: linewidth broadening and signal attenuation. It is well known that the susceptibility broadening can be removed effectively by magic angle spinning (MAS). Liquid state MAS permits high-resolution spectroscopy of complex samples [49]. Furthermore, our study has shown that MAS may also suppress the signal attenuation due to molecular diffusion in background gradients.

Background Gradients under MAS

While the shape and size of the overall field distribution is very geometry dependent within a heterogeneous sample, the susceptibility induced local fields may be considered dipolar[16]. Andrew [3] described the frequency modulation of a spin in a dipolar field under MAS. When spun at a frequency ω_r, the z component of the magnetic field at a point $\vec{r}$ from a dipole $\vec{\mu}$ located at the origin, is given by,

$$
\begin{aligned}
B_z(\vec{r}, t) = {} & \frac{\vec{\mu}}{r^3}[(3cos^2\theta - 1)(3cos^2\beta - 1) + \frac{3}{2}sin2\theta sin2\beta cos(\omega_r t + \phi) \\
& + \frac{3}{2}sin^2\theta sin^2\beta cos(2\omega_r t + 2\phi)],
\end{aligned}
\tag{2.6}
$$

where θ is the angle between the spinning axis and the static magnetic field. The point of interest is defined by two additional angles, β the angle between $\vec{r}$ and the spinning axis, and ϕ the angle out of the (y,z) plane which includes the spinner axis (Fig. 2-7).

37

At the magic angle $cos\theta = \sqrt{\frac{1}{3}}$, the modulation field has a purely sinusoidal dependence,

$$B_z(\vec{r}, t) = \frac{\vec{\mu}}{r^3}[\sqrt{2}sin2\beta cos(\omega_r t + \phi) + sin^2\beta cos(2\omega_r t + 2\phi)]. \qquad (2.7)$$

The well known result that MAS averages dipolar interactions to zero is seen by taking the time-averaged value of Eq. 2.7, which is zero for times long compared to the rotation period. It is this result that Garroway [16] built upon to show that in the static case, MAS removes the excess spectral broadening from susceptibility fields.
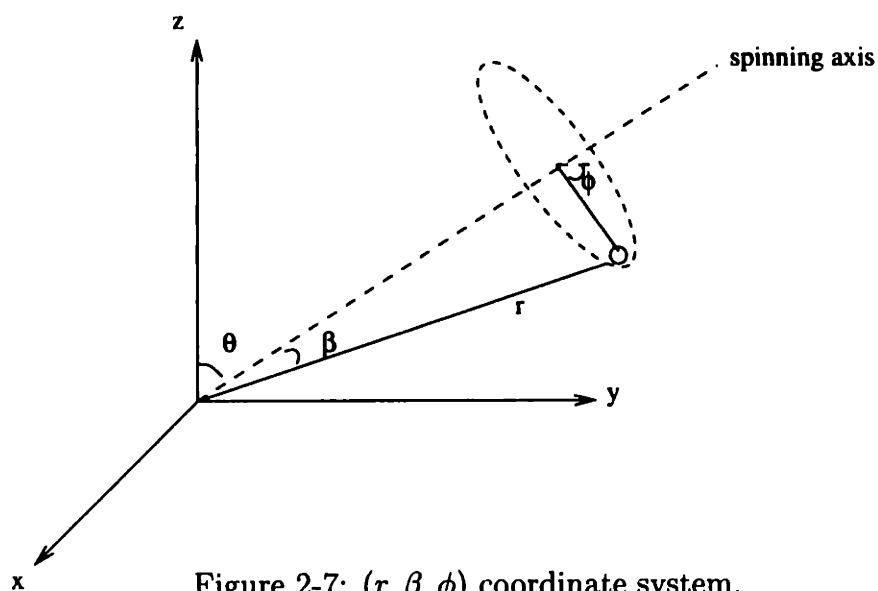
Figure 2-7: (r, β, ϕ) coordinate system.

Dynamic Averaging of Background Gradients

Although magic angle spinning averages time-independent dipolar field to zero, including those created by susceptibility variations in heterogeneous samples, spectral frequency variations introduced by random diffusive motions through the magnetic field gradient interferes with this averaging. Here we describe the competition between the coherent averaging introduced by the sample rotation and the stochastic averaging introduced by molecular diffusion [20]. Perhaps a convincing picture of the spin dynamics under MAS can be made through comparison to the coherent averaging

available through Carr-Purcell (CP) type pulse sequences. However, it is important to remember that, with MAS the strength of the background gradients themselves are being modulated and not the spin states of the system as in the multiple-pulse experiments. This implies that the details of the averaging are fundamentally different for the two cases. Under MAS, the Hamiltonian describing the susceptibility shifts may change in strength and sign as function of time, but it commutes with itself at all instances (which is not to say that the total spin Hamiltonian commutes at all times). In the CP sequence, the strength of the local interaction is constant and the spin dependence of the Hamiltonian is modulated. Therefore, the averaging, introduced by MAS of the susceptibility Hamiltonian, is a simple linear time averaged evolution, and the simplicity of the experiment and the lack of artifacts reflect this. At high spinning rates, the effect of the background gradients is predictably eliminated.

In order to explore the time-dependent cases, it is convenient to expand the local field into gradient terms to introduce a length scale suitable for comparison to molecular displacements. This is straightforwardly done by taking a linear approximation to the field at every point in space,

$$B_z(\vec{r} + \Delta\vec{r}) = B_z(\vec{r}) + \vec{g}(\vec{r}) \cdot \Delta\vec{r}. \tag{2.8}$$

In the (r, β, ϕ) coordinate frame, the local gradient is

$$\vec{\Delta} = \hat{r}\frac{d}{dr} + \hat{\beta}\frac{1}{r}\frac{d}{d\beta} + \hat{\phi}\frac{1}{r\sin\beta}\frac{d}{d\phi}. \tag{2.9}$$

Without loosing generality, we can explore the gradient in the neighborhood of $\phi = 0$, so that the local gradient of the time-dependent susceptibility field spun at the magic angle is,

$$
\begin{aligned}
\vec{g}(\vec{r}, t) \ = \ & \hat{r}\frac{\mu}{r^4}[-3\sqrt{2}sin2\beta cos(\omega_r t) - 3sin^2\beta cos(2\omega_r t)] \\
& + \ \hat{\beta}\frac{\mu}{r^4}[2\sqrt{2}cos2\beta cos(\omega_r t) + sin2\beta cos(2\omega_r t)] \\
& + \ \hat{\phi}\frac{\mu}{r^4}[-2\sqrt{2}cos\beta sin(\omega_r t) - 2sin\beta sin(2\omega_r t)].
\end{aligned} \tag{2.10}
$$

The echo attenuation observed in the presence of a magnetic field gradient is a result of a competition between the spin magnetization being wound into a spatial helix whose wave number, k, depends on the local field gradient,

$$\vec{k}(\vec{r}, t) = \gamma \int_0^t \vec{g}(\vec{r}, t')dt', \tag{2.11}$$

and the spins randomly moving through the gradient at a rate given by the diffusion constant, D. In the case of free molecular diffusion, the overall echo attenuation, A, is,

$$A(t) = exp(-D \int_0^t |\vec{k}|^2(t')dt'). \tag{2.12}$$

The motion of the spins through the local gradient field is isotropic and an explicit expression for the attenuation depends only on the magnitude of the k-vector, not its orientation,

$$|\vec{k}|^2 = \frac{\gamma^2\mu^2}{r^8\omega_r^2}[A_0 + A_1 \cos(\omega_r t) + A_2 \cos(2\omega_r t) + A_3 \cos(3\omega_r t) + A_4 \cos(4\omega_r t)], \tag{2.13}$$

where

$$A_0 = \frac{879}{64} + 2\sqrt{2}\sin 2\beta + \frac{75}{16}\cos 2\beta - \frac{155}{64}\cos 4\beta; \tag{2.14}$$

$$A_1 = -8 + \frac{5\sqrt{2}}{4}\sin 2\beta - 8\cos 2\beta - \frac{5\sqrt{2}}{8}\sin 4\beta; \tag{2.15}$$

$$A_2 = \frac{-11}{2} - 2\sqrt{2}\sin 2\beta + 3\cos 2\beta + \frac{5}{2}\cos 4\beta; \tag{2.16}$$

$$A_3 = -\frac{5\sqrt{2}}{4}\sin 2\beta + \frac{5\sqrt{2}}{8}\sin 4\beta; \tag{2.17}$$

$$A_4 = -\frac{15}{64} + \frac{5}{16}\cos 2\beta - \frac{5}{64}\cos 4\beta. \tag{2.18}$$

The echo signal both oscillates at harmonics of the spinning speed and decays over time:

$$A(t) = exp(-\frac{\gamma^2\mu^2}{r^8\omega_r^2}A_0Dt) \tag{2.19}$$

$$\times \quad exp[-\frac{\gamma^2\mu^2}{r^8\omega_r^3}D(A_1\sin\omega_r t + \frac{1}{2}A_2\sin 2\omega_r t + \frac{1}{3}A_3\sin 3\omega_r t + \frac{1}{4}A_4\sin 4\omega_r t)].$$

The exponential decay of the first term in the expression given above depends both on geometrical factors and the spinning rate. This first term is the most interesting, since it shows an exponential decrease of the signal over time and dominates at higher spinning rates. The exponential time constant is proportional to the spinning speed squared and thus at higher speeds we expect less attenuation.

The modulation of the spin magnetization and the expression for the echo attenuation are reminiscent of those for a Carr-Purcell sequence of π pulses separated by an interval (τ) or repeated at a frequency $\nu_p = \tau^{-1}$:

$$A_{cp}(\tau) = exp(-\frac{\gamma^2 g^2 D}{3\nu_p^2}\tau), \tag{2.20}$$

in which g is the gradient strength.

From the $\vec{k}$ expression, we can see that spinning the sample causes the k trajectory to be sinusoidally modulated, while the k trajectory in a CP experiment is a triangular modulation. The resultant signal attenuation curves are shown in figure 2-8. Here it is clearly seen that the oscillatory terms do not contribute in the high frequency regime where MAS is useful for averaging the susceptibility shifts.

Some of the advantages of using MAS methods rather than CP sequences to average the effects of susceptibility fields include:

1. the averaging is in spatial degrees of freedom so that the isotropic parts of other linear I_z Hamiltonians (such as the chemical shift) are not averaged by MAS and pulsed spin-locking type effects are avoided;

2. MAS is compatible with pulsed gradient spin echo sequences for measuring molecular diffusion rates;

3. the averaging of the susceptibility Hamiltonian is truly a first order effect for MAS, since the Hamiltonian commutes with itself at all times.
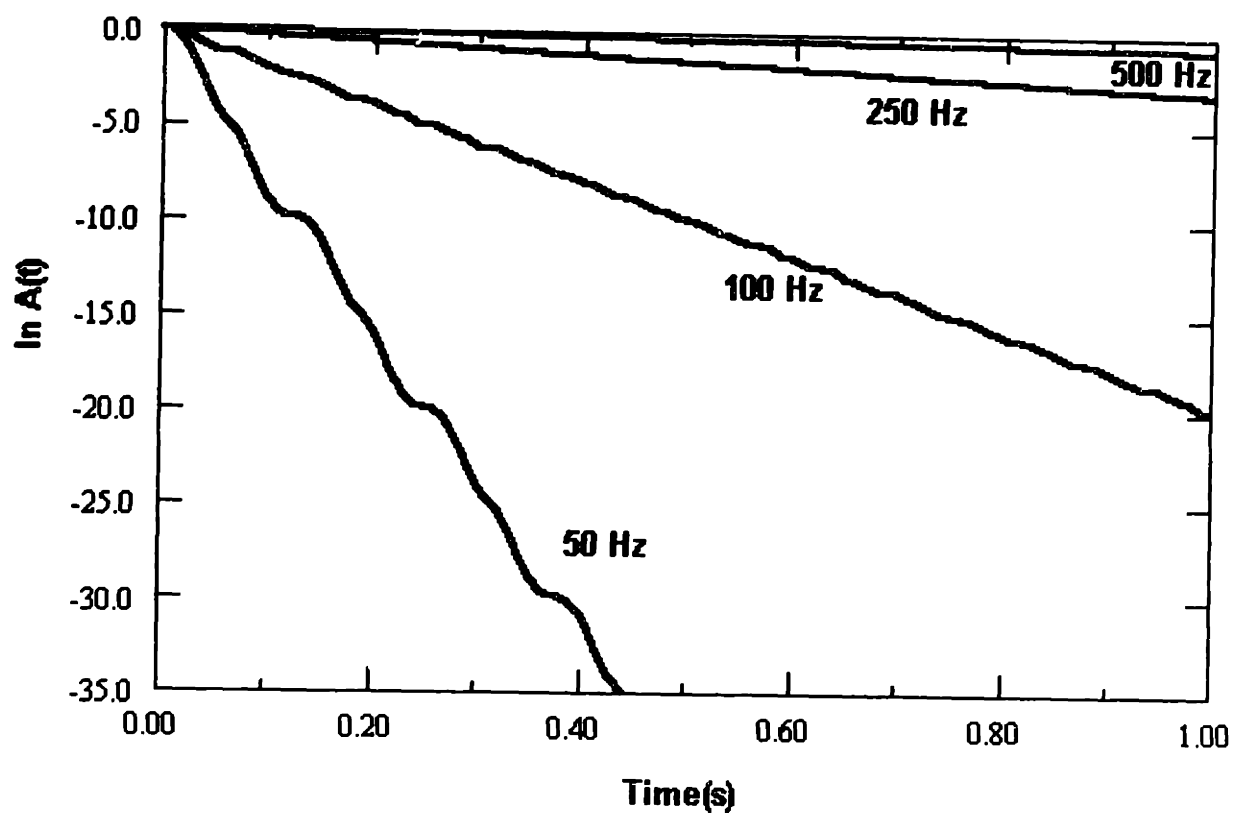
Figure 2-8: Plot of the attenuation vs. time according to Eq.2.19, calculated at four different magic angle spinning speeds. A background gradient of $100T/m$ is assumed and the diffusion constant is approximately that of water $(3 \times 10^{-9} m^2/s)$.

Experimental Results

Effects of MAS on Pulsed Gradient Stimulated Echo (PGSTE) and Carr-Purcell-Meiboom-Gill (CPMG) measurements were tested. Figure 2-9 compares CPMG and MAS averaging of the echo attenuation for a water proton T_2 measurement in a slurry. The slurry was created by wetting aluminum oxide (400 mesh) with water. The experiments were obtained on a Bruker Avance spectrometer, operating at a proton frequency of 500MHz. The echo intensities were acquired at intervals of $4ms$, under both static and spinning conditions, and for varying π-pulse spacing τ. In the static case, smaller τ values lead to less attenuation due to the partial averaging of the susceptibility induced background gradients. Under MAS the background gradients are averaged out and the attenuation curves become independent of τ. Figure 2-10 shows the effect of MAS on a diffusion measurement. A high resolution MAS probe was used, which is equipped with a magic angle gradient, capable of generating $5G/cm$ per Ampere [33]. The diffusive curves were obtained with a PGSTE sequence under both static and spinning conditions, and with two values of the diffusion time Δ. In a heterogeneous sample the background gradients, caused by differences in the local magnetic susceptibility, lead to erroneous diffusion attenuation curves. In a constant time stimulated echo experiment the apparent diffusion coefficient is smaller due to the interaction between the background gradients and the applied gradients. In addition, under these conditions differences in stimulated echo decay are observed between experiments obtained with different values of Δ [13, 29, 28]. Under MAS the background gradients are averaged and the diffusion curves become independent of the value of Δ used.

Conclusion

In this section, we have shown both theoretically and with experimental examples that MAS not only averages the static effects of susceptibility fields, but that is also averages the dynamic influences, provided that the spinning rate is sufficiently fast. We expect that this will become the method of choice for studies of the diffusion

behavior in heterogeneous samples. In separate measurements, we have seen that MAS will return a broadened line due to spectral diffusion in a broad magnetic field gradient to a narrowed resonance. This is an example of MAS line narrowing applied to the fast motion limit. Finally, we anticipate that sideband analysis in slow MAS will permit a direct measurement of the strength of the background gradients in a sample.
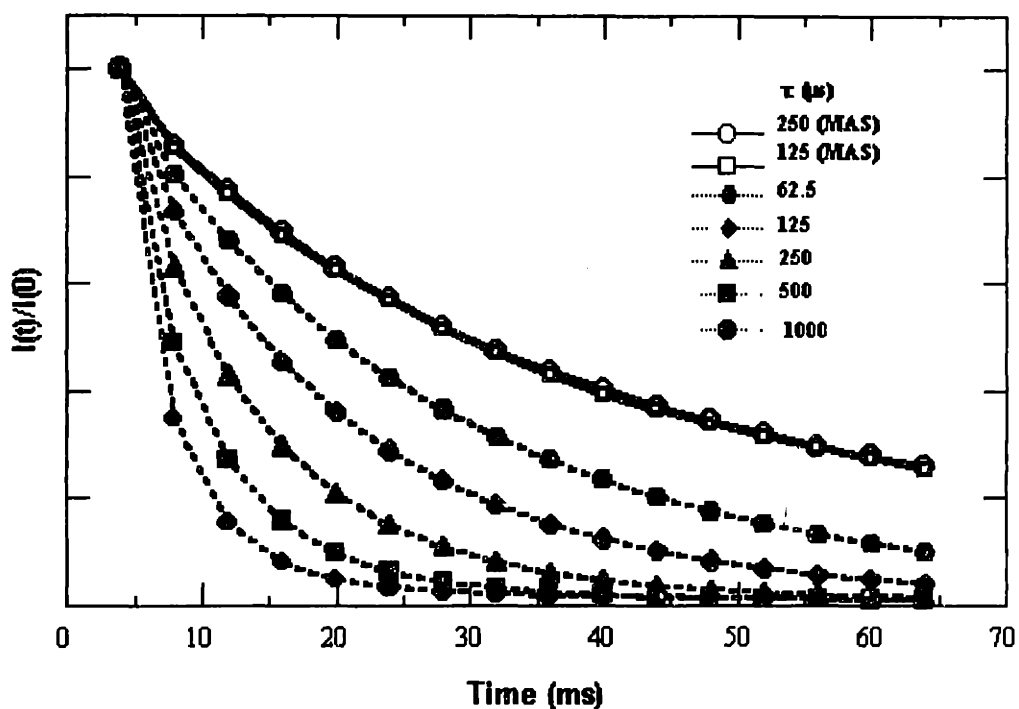
Figure 2-9: Echo attenuation curve of the water protons of an aluminum oxide slurry, obtained in a CPMG experiment. The different curves are obtained with a range of τ-values, as well as with or without magic angle spinning. In the static case, smaller τ values lead to less attenuation due to the partial averaging of the susceptibility induced background gradients. Under MAS the background gradients are averaged out and the attenuation curves become independent of τ.
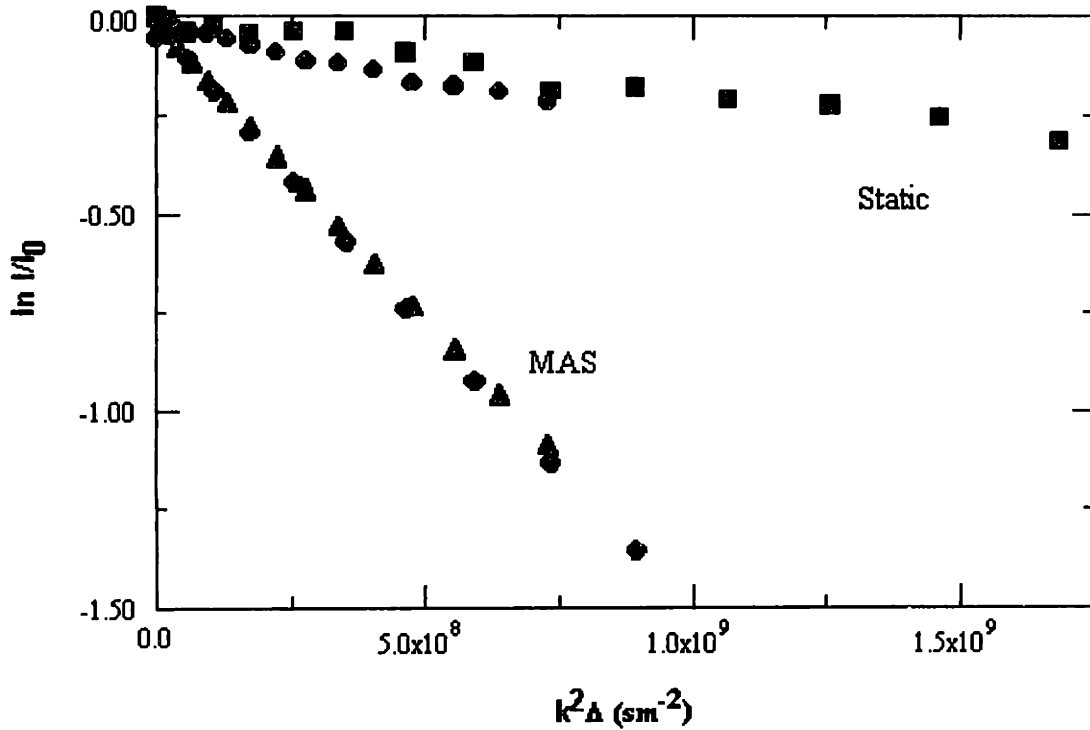
Figure 2-10: Diffusion attenuation curves of water in an aluminum oxide slurry. The diffusion experiments were performed under MAS $(4000Hz)$ and static conditions and as a function of two different diffusion times Δ. Due to the presence of a susceptibility induced background gradient, the static experiments yield an apparent diffusion coefficient D which differs significantly from the true diffusion constant and which is furthermore dependent on Δ. MAS averages the background gradients, resulting in the correct measurement of the diffusion coefficient, which is no longer dependent on Δ.

Chapter 3

Constant Time Imaging (CTI) Approaches to NMR Microscopy

The resolution in NMR microscopy is limited by a combination of the inherent low sensitivity of NMR, the intrinsic spectral line-width, the destruction of spin magnetization gratings by molecular diffusion, and the local magnetic field variations introduced by bulk susceptibility. While none of these may be completely overcome, constant time imaging (CTI) approaches are optimal (best SNR per unit time) for recording images when the above factors are important [17, 12]. In this chapter, CTI approaches are introduced, analyzed in the presence of molecular diffusion and background gradients, and demonstrated to yield high-resolution images.

3.1   3D CTI

CTI was introduced in 1985 by Emid and Creyghton [15] for solid state imaging, where the broad dipolar line-width greatly reduces the image resolution and sensitivity. CTI employs phase encoding in all spatial directions, with only a single data point being collected per excitation. Since the magnetic field gradients commute with all internal Hamiltonians and since only gradients are varied from acquisition to acquisition, the evolution of spins due to those time-independent Hamiltonians including the chemical shift, magnetic susceptibility, and dipolar coupling is constant and, therefore,

unobserved. The image resolution is determined solely by k-space sampling, molecular diffusion, and sensitivity considerations. In liquid-state imaging, CTI has advantages over frequency encoding imaging methods in two aspects: narrow intrinsic spectral line-width and much less signal attenuation due to molecular diffusion when strong pulsed gradients are used.

Fig. 3-1 shows a basic 3D CTI pulse sequence in comparison with a standard spin-warp sequence, 3D Spin Echo Imaging(SEI). In NMR microscopy, it is generally difficult to obtain a high quality 2D slice selected image. There are pronounced sensitivity losses during the slice selection process due to diffusion when the slice thickness is less than $40\mu m$ (see section 2.1.2). Where the sample has a known symmetry that permits the in-plane resolution to be substantially higher than the slice thickness, anisotropic voxels are useful; otherwise, 3D imaging must be used.
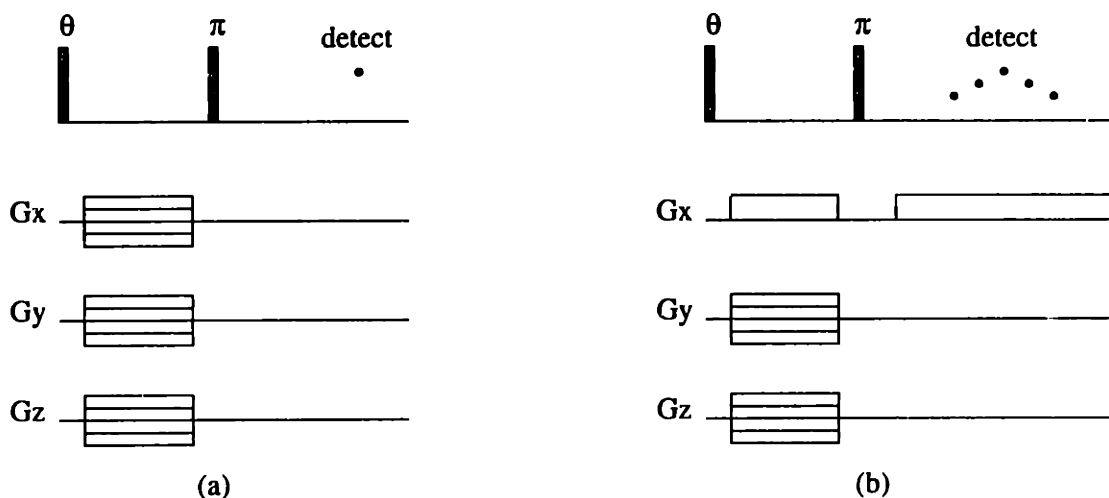
Figure 3-1: (a) 3D CTI sequence. Phase-encoding is used along all spatial directions. (b) 3D SEI sequence. Frequency-encoding is used along one of the spatial directions.

Since CTI uses phase encoding in all three spatial directions, it is very time consuming. This is perhaps the major drawback of CTI and has severely limited its use in NMR imaging. For a repetition time T_R, it requires a total experimental time of $N^3 \times T_R$ to record an image of $N \times N \times N$ voxels with CTI, which is N times

longer than in SEI or other imaging methods employing frequency encoding. Therefore, shortening experimental time along with sensitivity enhancement are the central goals in CTI sequence optimization. There are three options available: (a) reduce the repetition time to the minimum possible, (b) reduce the number of sampled points, and (c) maintain sufficient sensitivity that signal averaging is not required [8]. In what follows, they are discussed one at a time.

3.2 Ernst Angle

In order to keep 3D imaging experiments reasonably short, it is essential to have fast repetition. The limit on the repetition time is often set by the maximum duty cycle (see p.65) of the gradient set rather by spin-lattice relaxation considerations. The time interval between adjacent excitation pulses can be much less than the time taken for the full recovery of longitudinal magnetization. In this case, the spin system establishes a dynamic equilibrium. For a repetition time T_R and spin-lattice relaxation time T_1, the transverse magnetization immediately after each RF pulse with a tip angle θ is,

$$M_y = M_0 \frac{1 - exp(-T_R/T_1)}{1 - cos\theta exp(-T_R/T_1)} sin\theta, \qquad (3.1)$$

where M_0 is the longitudinal magnetization at thermal equilibrium [6]. Therefore, the signal amplitude ($\propto M_y$) is maximized when θ equals to a value known as the Ernst angle, θ_E, for which

$$cos\theta_E = exp(-T_R/T_1). \qquad (3.2)$$

For T_R/T_1 of around 3, the relaxation between pulses is fairly complete and the Ernst angle is close to 90°. Fig. 3-2 shows the signal-to-noise advantage of using Ernst angle pulses over 90° pulses for short T_R's. Unfortunately, no matter what repetition time and turn angle employed, the T_1 relaxation time provides a fundamental limit to the available SNR. This in turn limits the practical use of CTI and the possible spatial resolution in NMR microscopy. Also, it should be noted that heterogeneous samples, such as small living organism and tissues, usually possess multi-T_1 components. The

RF pulse tip angle is often chosen so as to provide an optimal T_1 contrast (Fig. 3-3).
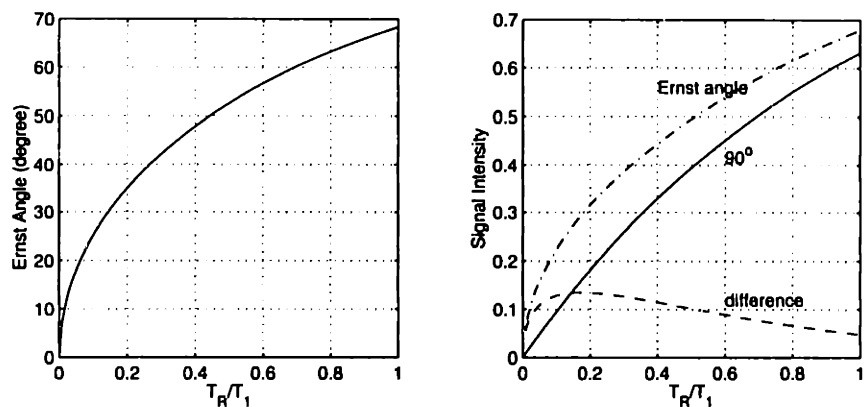
Figure 3-2: (a) Ernst angle vs. repetition time. (b) SNR advantage of Ernst angle over 90 pulse.
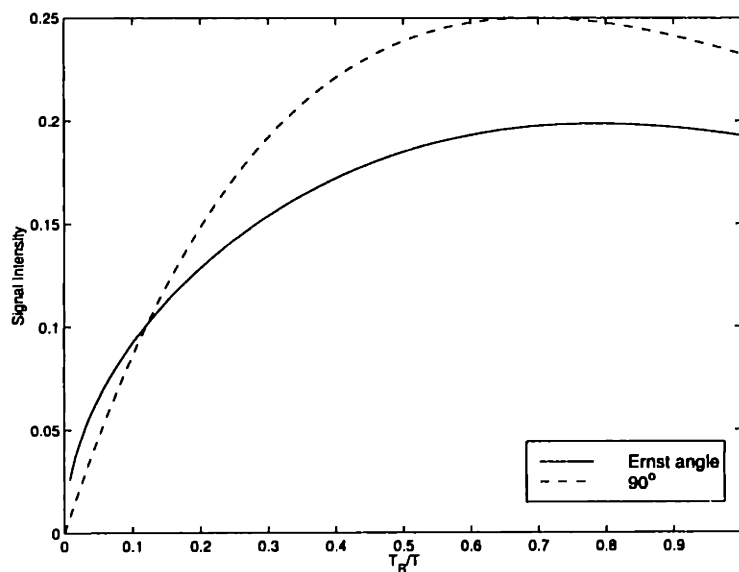
Figure 3-3: Intensity difference of NMR signals originated from two compartments with different T_1's, T and $2T$. It varies as a function of the repetition time T_R and tip angle. The two compartments are assumed to contain the same number of spins.

3.3 CP Detection

In NMR imaging, sampling time after each excitation is usually much shorter than T_2, the spin-spin relaxation time. So there is some residual transverse magnetization that can be used repetitively. However, the phase coherence of the transverse magnetization will be lost after several T_2^*'s. Successive recoveries of the phase coherence are possible only if a train of 180° pulses, the so called Carr-Purcell (CP) sequence, is applied. Co-addition of the echoes generated in CP sequence leads to a significant signal-to-noise enhancement without lengthening of imaging experiments, which is ideal for CTI [1]. Signal averaging from successive experiments is practically impossible in CTI, since each scan takes a long time. Fig. 3-4 shows the pulse sequence of 3D CTI combined with CP coherent averaging detection. The choice of phase with which these 180° pulses are applied is important. Acceptable CP pulse trains must compensate for pulse imperfections. Pulse imperfections come from many sources such as phase glitches, improper pulse length, RF amplitude imbalances and etc. Furthermore, in order to employ Ernst angle pulses, the longitudinal magnetization M_z must be well preserved prior to excitation. There are a number of Carr-Purcell-like pulse sequences developed in early 1990's to eliminate artifacts associated with pulse errors [44, 19]. Among them, XY-based sequences, as shown in this table, were proven to have superior performance [18], especially in preserving M_z.

sequence name	RF phases
XY-4	$(xyxy)^n$
XY-8	$(xyxyyxyx)^n$
XY-16	$(xyxyyxyx\bar{x}\bar{y}\bar{x}\bar{y}\bar{y}\bar{x}\bar{y}\bar{x})^n$

Table 3.1: Phases of 180° pulse train

---

[1]See section 1.3 for the introduction of spin echo and signal averaging.

Sensitivity Enhancement

The signal-to-noise ratio in a basic 3D CTI sequence as shown in Fig. 3-1 is:

$$SNR_0 = \frac{S_0 e^{-\tau/T_2}}{N_0},\qquad(3.3)$$

where S_0 is the signal amplitude immediately after excitation, N_0 is the r.m.s noise of one data point, and τ is the spin echo time. For a given NMR probe and temperature, the noise (white noise) depends only on the detection bandwidth Δf. Therefore,

$$N_0 = C\sqrt{\Delta f},\qquad(3.4)$$

where C is a constant independent of measurement technique. In CTI, Δf is equal to $(\pi T_2^*)^{-1}$, on the order of $100Hz$. So the acquisition dwell time T is usually a few milliseconds which determines the minimum spacing between adjacent π pulses. With CP detection, the signal-to-noise ratio is,

$$SNR_{CP} = \frac{\sum_{i=1}^{n}\sum_{j=1}^{m} S_0 e^{-i\tau/T_2} e^{-|j-(m+1)/2|\cdot T/T_2^*}}{\sqrt{m\cdot n}\cdot N_0},\qquad(3.5)$$

where n and m are the number of echoes and the number of points collected per echo. Here, the detection of each echo is assumed to be symmetric and m is odd. The minimum spin echo time τ is taken to be $(m+1)T$. The sensitivity enhancement by multi-echo detection is significant only if $T_2 >> T_2^*$. In which case, m is set to be one. However, when T_2 and T_2^* are close, then multi-point-single-echo ($n = 1$) or FID detection is more efficient. Figure 3-5 shows the sensitivity enhancement as a function of T_2^*/T_2 with optimized m and n. The detection bandwidth is fixed to be $500Hz$.

CP coherence detection was tested on a phantom, a cylinder of doped water ($25mM\ CuSO_4$) with a diameter of $100\mu m$. This sample has a T_2 of $100ms$, and T_2^* of $45ms$. A portion of the cylinder ($100\mu m$) is slice selected for 3D imaging. Center slices of the 3D images reconstructed from single point detection and CP detection are shown in Fig. 3-6(a) & (c). The two images were acquired under the

51

same experimental conditions and within the same experimental time. Both images have an in-plane resolution of $2\mu m \times 2\mu m$, and a resolution of $8\mu m$ along the cylinder axis. The total experiment time for acquiring each 3D image was $4hrs$ and $30mins$ with a FOV of $(128\mu m)^3$. With 20 point CP detection, the SNR is improved by a factor of 3.
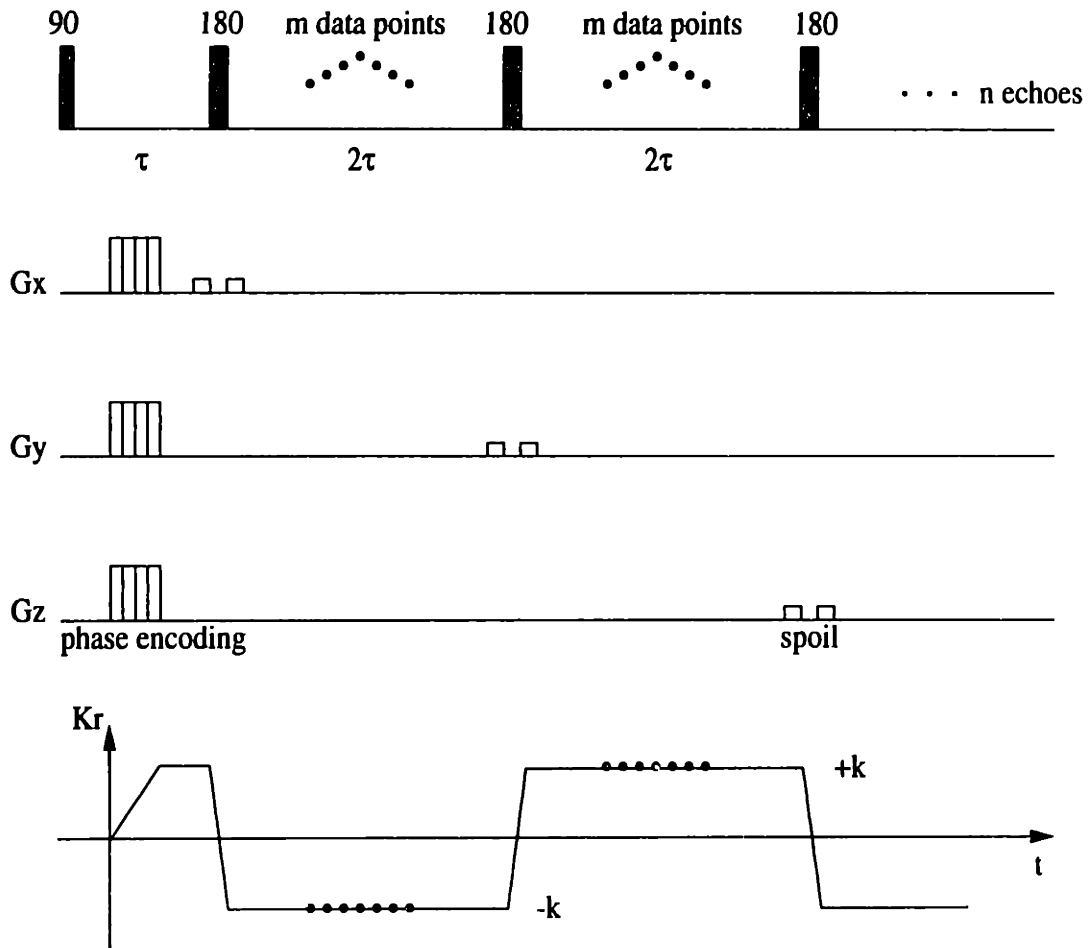
Figure 3-4: 3D CTI sequence with CP coherent averaging detection.
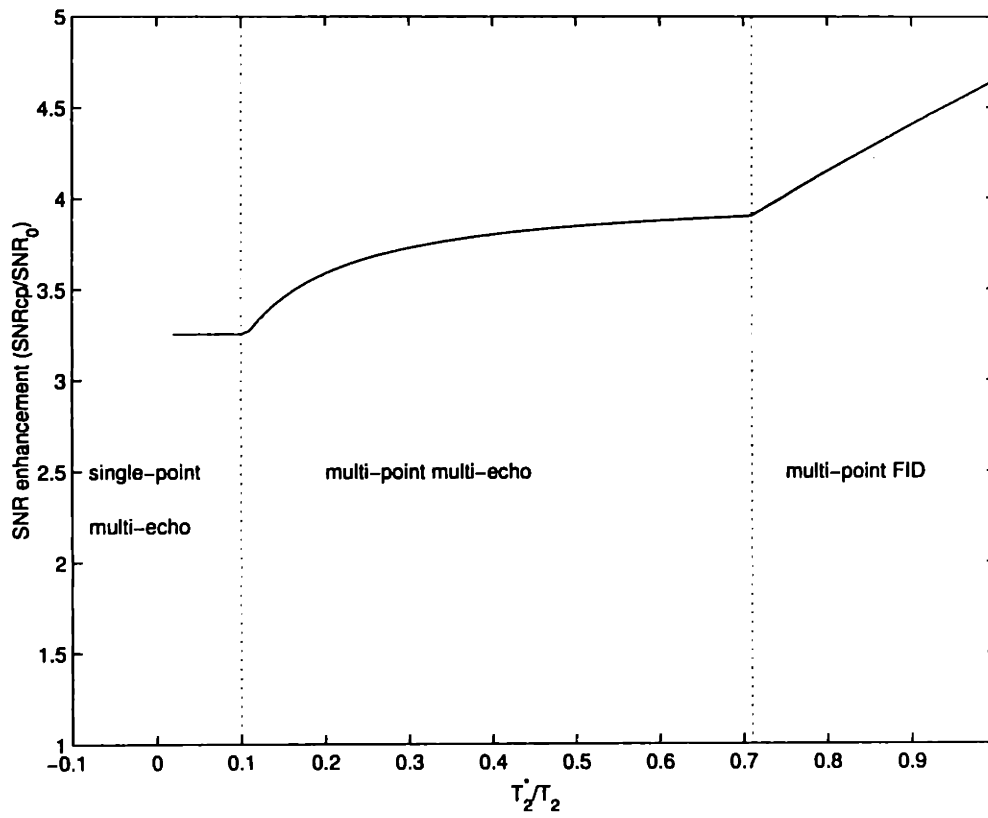
Figure 3-5: SNR enhancement by CP coherent detection. T_2 equals to $100ms$ is used in the calculation.
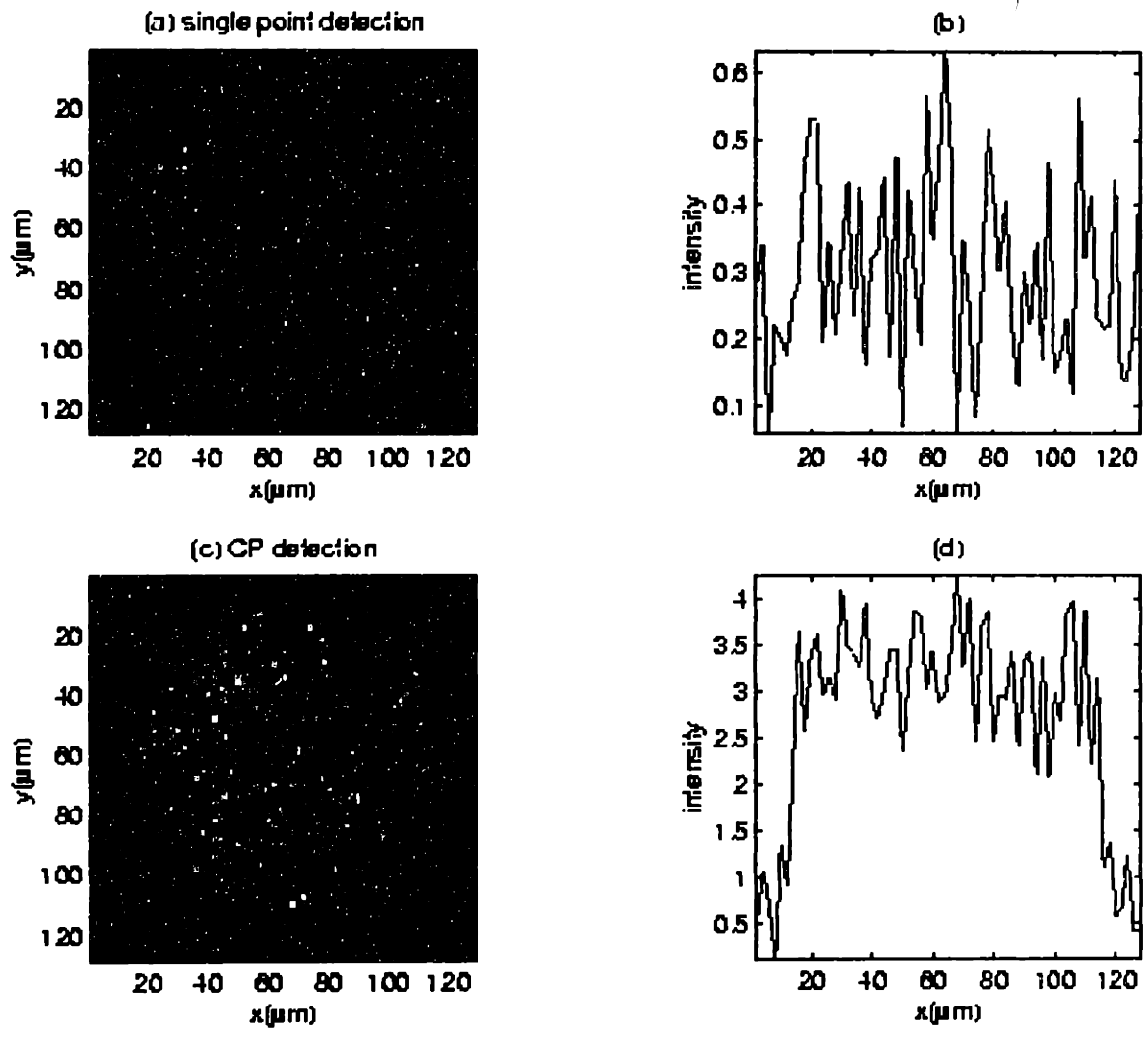
Figure 3-6: Center slices of the 3D images reconstructed from single point detection (a) and CP detection (c). (b) and (d) are the intensity plots of the center lines in (a) and (c) respectively. A SNR enhancement of 3 is achieved by a 20 point CP detection.

54

3.4   Reduced K-Space Sampling

As described in the previous sections, experiment time in CTI can be reduced by using shorter T_R and no signal averaging from successive scans. Unfortunately, even with the shortest T_R, which is about $100ms$, hours are necessary for a single scan. As an example, acquiring a 3D image of $64 \times 64 \times 64$ voxels requires $7.3hrs$. Further shortening of the experiment time therefore depends on reducing the number of data points while maintaining a desired resolution and field-of-view (FOV). In this section, the total experimental time, PSF's, and sensitivity of CTI with a reduced k-space sampling scheme are discussed in detail. It is shown that this spherically truncated sampling method is effective in both reducing the total experimental time and enhancing SNR, while introducing no additional blurring or distortions to the image reconstructed.

To record an image at a given resolution, the range of k-space to be sampled is fixed by the Nyquist condition. Conventionally, a cube from $(-k_m, -k_m, -k_m)$ to (k_m, k_m, k_m) in k-space is sampled on a Cartesian raster to reconstruct a 3D image with isotropic voxels and FOVs. In spherically truncated sampling, only the volume within a sphere of radius k_m is sampled. Therefore, the total number of data points is reduced to $\frac{\pi}{6}N^3$, about half that of cubic sampling, and the experimental time is also cut in half. With a $100ms$ repetition time, the total experimental time for acquiring a 3D image of $64 \times 64 \times 64$ voxels is reduced to $3.8hrs$ with spherically truncated sampling. The data points are still sampled on a Cartesian raster, and the induced broadening of the Point-Spread-Function (PSF) by the reduced k-space sampling is negligible. In addition, a gain in SNR is achievable due to the dominant noise level at the high k corners.

Point Spread Function (PSF)

NMR images are normally reconstructed from a complete set of data points in k-space, which are the spatial Fourier components of the sample's spin density, $\rho(x, y, z)$. Employing the Weiner-Kintchine theorem of Fourier convolution, the truncation and

diffusive attenuation in k-space may be added as major contributors to the PSF in CTI,

$$Image = \rho(x, y, z) \otimes PSF_{truncation} \otimes PSF_{diffusion} + Noise. \qquad (3.6)$$

The PSF's blur the image and hence reduce the spatial resolution. The $PSF_{truncation}$ from cubic sampling (PSF_{CS}) and spherical sampling (PSF_{SS}) are,

$$PSF_{CS} = Sinc(k_m x)Sinc(k_m y)Sinc(k_m z), \qquad (3.7)$$

$$PSF_{SS} = \frac{1}{r^3}[Sin(k_m r) - k_m r Cos(k_m r)]. \qquad (3.8)$$

According to the Nyquist condition, the resolution along all three directions is $\Delta = \frac{\pi}{k_m}$, which is exactly the period of PSF_{CS}. Thus, all data points (except the origin) fall on the zero-crossings of the $Sinc$ functions which make up the PSF_{CS}, and Gibbs ringing is not observed. The spherically sampled point spread function, PSF_{SS}, on the other hand, is not periodic. Figure 3-7 shows both PSF_{CS} and PSF_{SS}. As seen in the figure, however, both the additional broadening and the Gibbs ringing given by the reduced k-space sampling are negligible. The amplitude of Gibbs ringing in PSF_{SS} is within a few parts in 10^4 of the center peak intensity.

Diffusive signal attenuation in the case of phase encoding is given by [6],

$$A(\vec{k}) = exp(-\frac{\mid \vec{k} \mid^3 D}{3\gamma G_m}) \qquad (3.9)$$

where, D is the diffusion constant, G_m is the gradient strength. Here, the constant strength phase encoding method is used. $PSF_{diffusion}$, the 3D inverse Fourier transform of $A(\vec{k})$, is the single most important contributor to the overall PSF as shown in Figure 3-8. Since $\mid \vec{k} \mid$ is maximum in the corners, attenuation is maximum as well.
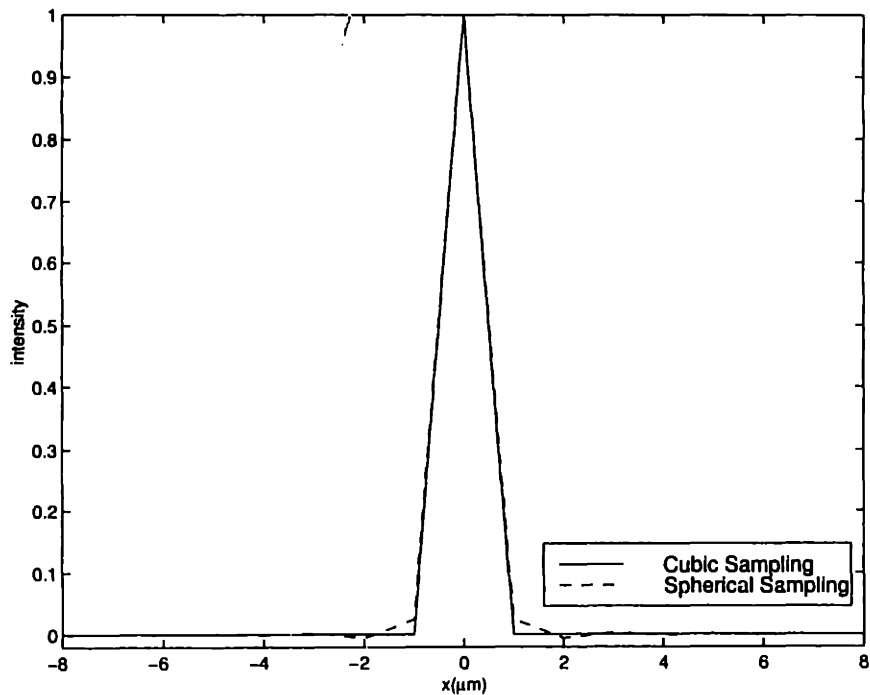
Figure 3-7: Center lines (x, y=0, z=0) of PSF's. PSF_{CS} and PSF_{SS} have the same FWHM of $1\mu m$. The Gibbs noise in PSF_{SS} is within a few parts in 10^4 of the center peak intensity.
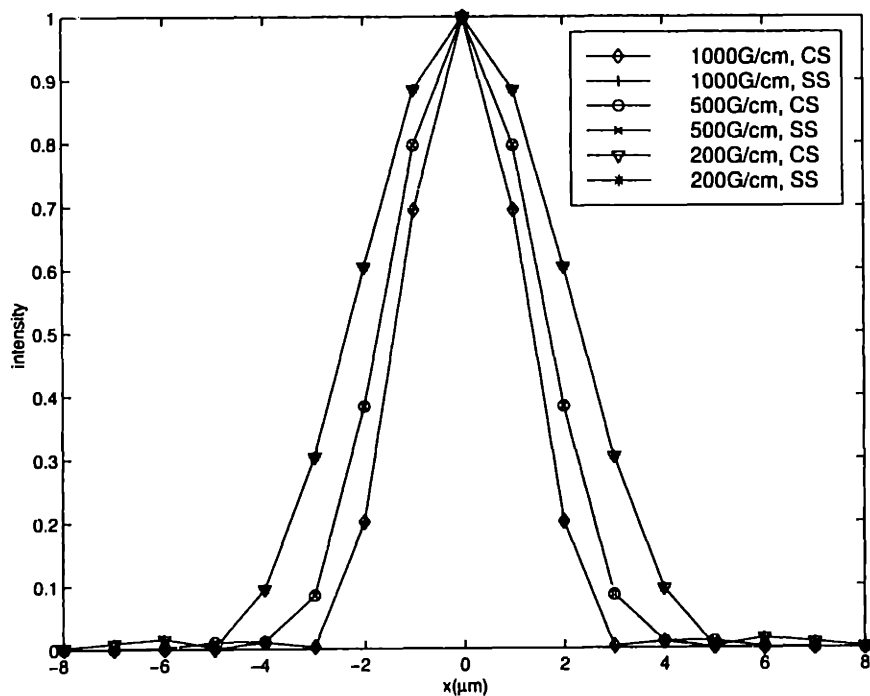
Figure 3-8: Center lines of PSF's (x, y=0, z=0) with diffusion. The diffusion constant for free water $(2.2\mu m^2/ms)$ is used in this simulation. For maximum phase encoding gradient strengths $200G/cm$, $500G/cm$, and $1000G/cm$, PSF_{CS} and PSF_{SS} are identical. Uneven diffusive attenuation in k-space is the dominant contributor to the overall PSF broadening.

Sensitivity

In order to compare the SNR of these two sampling strategies, we follow the procedure of Link and Seelig [32] and define the sensitivity as SNR per unit time, $sensitivity = \frac{S_T}{N_T\sqrt{T_T}}$, where S_T, N_T, and T_T stand for the total signal, noise (r.m.s.) and experimental time. The improvement of spherical sampling over cubic sampling in sensitivity is,

$$\frac{Sensitivity^{SS}}{Sensitivity^{CS}} = \frac{S_T^{SS}}{S_T^{CS}} \cdot \frac{N_T^{CS}}{N_T^{SS}} \cdot \sqrt{\frac{T_T^{CS}}{T_T^{SS}}} = 1 \cdot \sqrt{\frac{6}{\pi}} \cdot \sqrt{\frac{6}{\pi}} \approx 1.9. \qquad (3.10)$$

There is no signal loss due to the truncation of high k corners since the data point at the origin of k-space, which represents S_T, stays untouched. The noise involved in NMR experiments is assumed to be white noise. Both N_T^2 and T_T are proportional to the total number of data points sampled in k-space [8].

Experimental Results

CTI with both the cubic and spherically truncated sampling schemes were tested on a phantom: a small piece of fabric net was placed inside a $400\mu m$ capillary tube filled with water doped with $2mM$ Gd. The net consists of strings with $50\mu m$ diameter and $50\mu m$ squares between strings. There is no NMR signal contribution from the strings. The squares are occupied by water and appear to be bright in images. Figure 3-9(a)&(b) are representative slices taken from two 3D images reconstructed from the cubic and spherical sampled k-space data sets respectively. In the case of spherically truncated sampling, k-space data are zero filled to the same size as in cubic sampling. Both images were reconstructed by a direct Fourier transformation and then normalized. There is no blurring or SNR enhancement introduced by profile multiplication as usually taken in image processing. With reduced k-space sampling, the total experimental time is shortened from $16.5hrs$ to $8.6hrs$, and the SNR is enhanced by 1.36 times. So the total sensitivity improvement is 1.88, which is consistent with the theoretical prediction above. No observable resolution loss is associated with the spherical sampling as demonstrated in figure 3-9(c)& (d). The PSF for spherical

sampling on a Cartesian raster is narrower and more uniform in space compared to the PSF resulted from sampling on a polar raster as in projection reconstruction. There is no interpolation necessary and the image is less susceptible to distortions [30].

3.5 Conclusion

In NMR microscopy, diffusive signal attenuation and intrinsic low SNR are the ultimate limitations to resolution. With strong gradients around $1000G/cm$, the diffusion limited resolution is about $2\mu m$. Therefore, up to $2\mu m$, sensitivity is the major concern in acquiring high resolution images. In this chapter, I presented a modified CTI sequence, which combines strong gradients, Ernst angle, CP coherent detection, and reduced k-space sampling. By applying Ernst angle excitation pulses instead of 90° pulses, sensitivity can be enhanced by a factor of 2 for short repetition times ($\approx 0.2T_1$). Compared to basic CTI experiments, CTI with CP detection gives a dramatic SNR enhancement of 3 to 4.5 times. At the mean while, the total experiment time can be reduced to half since both $\vec{k}$ and $-\vec{k}$ components are sampled after a single excitation when even numbers of echoes are detected. Further more, with reduced k-space sampling as described above, an increase of 1.9 times is achievable in sensitivity. It is demonstrated that this new sequence makes it possible to acquire images with a high resolution of $2\mu m \times 2\mu m \times 8\mu m$ within a few hours.

Data Size	Resolution	FOV	T_R	Total Experiment Time	
				Basic CTI	CTI with CPMG & Reduced k-space
$(64)^2 \times 16$	$(2\mu m)^2 \times 8\mu m$	$(128\mu m)^3$	$200ms$	$3.7hrs$	$1hr$
$(128)^2 \times 32$	$(2\mu m)^2 \times 8\mu m$	$(256\mu m)^3$	$100ms$	$14.6hrs$	$3.8hrs$
$(64)^3$	$(8\mu m)^3$	$(512\mu m)^3$	$100ms$	$7.3hrs$	$2hrs$
$(128)^3$	$(8\mu m)^3$	$(1mm)^3$	$100ms$	$58.3hrs$	$15.3hrs$

Table 3.2: Experiment time in CTI
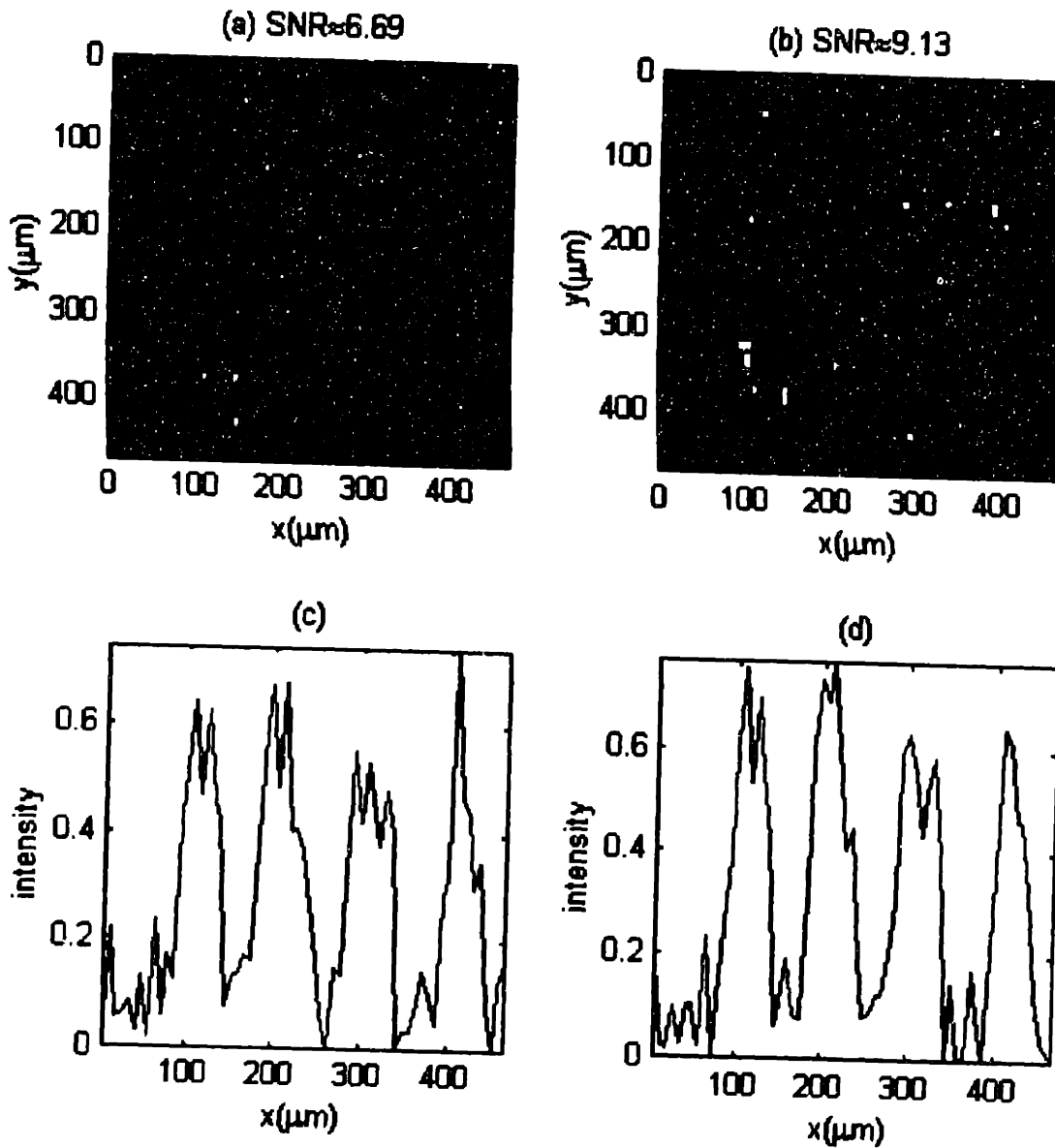
Figure 3-9: Identical slice taken from the 3D images generated by CTI with cubic (a) and spherically truncated (b) samplings of a mesh phantom described in the text. Both 3D images have a resolution of $(7.3\mu m)^3$. With $TR = 200ms$, the total experimental time was $16.5hrs$ for cubic sampling, and $8.6hrs$ for spherical sampling. The intensity plots at the marked position in (a) and (b) are shown in (c) and (d) respectively. The images are compared in terms of SNR and sharpness. A gain of 1.36 in SNR is achieved using the reduced k-space sampling.

Chapter 4

System Design

Micro-imaging has become one of the many standard options for commercial NMR spectrometers. However, all the commercial microscopes are developed for samples with a diameter of 5mm and up, while our interest is on smaller samples less than 2mm. Their instrumentation requirement are significantly different. The RF circuits in standard NMR probes are not optimized for detecting microscopic samples. Also, a strong gradient set ($\sim 1000G/cm$) is crucial for high-resolution imaging experiments. As part of my thesis work, a 600MHz system has been designed and constructed as a dedicated NMR microscope.

4.1   NMR Microscope Development

The successful implementation of high resolution imaging experiments requires new developments in radio frequency circuits and magnetic field gradients. A NMR microscope for a standard bore $14.1T$ magnet was developed, it is equipped with a small solenoidal RF coil and three orthogonal gradients with strengths of $1260G/cm$ for G_y, $760G/cm$ for G_z, and $410G/cm$ for G_x at $15A$.

4.1.1 Radio Frequency (RF) Circuit

The basic characteristics of an RF circuit are sensitivity, lineshape and B_1 homogeneity. Among these, sensitivity is the most important factor for a microscope, especially when CTI is used. In NMR microscopy, the sensitivity of the RF coil directly determines the minimum detectable number of spins. In another word, it determines the ultimate limit to resolution.

Among different coil geometries (e.g. solenoidal, saddle, birdcage, and surface coils), solenoid coils show the highest sensitivity and are commonly used in NMR microscopy [22]. We investigated the performance of solenoidal micro-coils as a function of coil diameter, number of turns, and wire diameter [11, 39, 37]. The sensitivity is enhanced when the diameter of solenoids is reduced while maintaining the coil length-to-diameter ratio. A set of solenoidal coils were fabricated by wrapping susceptibility matched wires directly around capillary tubes. Each tube was imbedded to a vaspel insert, which enabled the convenient exchange of RF coils according to sample size. The sizes and properties of these coils are listed in table 4.1. During the construction, most of the difficulties arise from the conflicting requirements that the coil be small to preserve a high filling factor, and yet at the same time all of the inductance of the circuit must be contained within the coil. The resistance should be insignificant. The circuit is normally remotely tuned with variable capacitors since the space in the gradient set is limited. The leads from the capacitors to the coil add stray inductance which lowers the efficiency. Also, at high frequencies variable capacitors are not high Q devices. We have developed a circuit that goes a long way in solving many of these problems. A high-quality, nonmagnetic chip capacitor is soldered directly across the RF coil inside the RF former. The two leads that connect this to the external variable tuning and matching circuit are kept as short as possible (Figure 4-2b).

coil diameter	90° pulse	sample size(diameter, length)
2.5mm	$5Watts, 5.4\mu s$	$1.9mm, 2.5mm$
1.5mm	$5Watts, 2.3\mu s$	$1.0mm, 2.0mm$
1.0mm	$5Watts, 1.5\mu s$	$600\mu m, 1.0mm$

Table 4.1: RF coils

One of the most useful measures of a RF circuits' efficiency is the power required to generate a 90° nutation. At $600MHz$, the 1.5mm coil requires only 5 Watts of power to generate a 90° pulse around $2\mu s$. The more traditional probes with coils of similar volumes require 25 Watts to generate a 90° pulse of $5\mu s$. This represents an improvement of more than 5 times in sensitivity. At higher frequencies and smaller coils the gain in efficiency will be even more pronounced.

4.1.2   Strong Magnetic Field Gradient Set

In NMR imaging experiments, spatial magnetization grating is generated by applying magnetic field gradients. Therefore, three orthogonal magnetic field gradients $G_x = dB_z/dx$, $G_y = dB_z/dy$, and $G_z = dB_z/dz$ are required. In addition, these gradients must satisfy some special requirements for NMR microscopy. They must be strong enough to limit the diffusive attenuation due to random molecular motions through a magnetization grating. At the same time the gradient set must switch fast enough to permit narrow bandwidth detection. From a practical point of view, the gradient set must fit inside the NMR magnet, must not introduce excessive eddy currents, must be efficiently cooled so as not to heat the sample, and must be mechanically stable (even when pulsed in the presence of a very strong static magnetic field).

In the microscope developed in this research, we built upon Choi's gradient coil design for a standard bore $400MHz$ system [11]. The geometries of the gradient coils have been calculated first based on a spherical tensor expansion of idealized coils [46], and then by Biot-Savart theory for actual coils [41]. In this fashion, the linearity and efficiency of the coils are precisely known prior to construction. The gradient coils G_y and G_z are small quadruple coils, and G_x is a Golay coil. This design has two advantages: first, the coils are wrapped on a cylinder that is transverse to the main magnetic field which easily accommodates a very efficient solenoid RF circuit; second, the gradients do not couple strongly to the main magnetic field hence reducing eddy currents, which is a result of the field symmetry and the small size. The gradient set in standard NMR probes is commonly right against the probe cover.

Fig. 4-1 shows the schematic diagram of current paths of the gradients. G_z has

two current paths per quadrant at 30° and 60° positions and all current paths are connected by return paths which are not shown in the diagram. G_y is obtained by rotating G_z by 45° around the x-axis. G_x is a simple Golay coil with $K = 0.4R$, $K_r = 1.64R$, where K, K_r and R are the postions and radius of the center and return arcs. The arcs subtend an angle of 120°. The number of copper wires per current path are 8 in G_z, 10 in G_y, and 8 in G_x and the wire diameter is $0.32mm$. The radius of the current paths, which is the distance from the origin of the axis to the bottom of the current paths, are $3.57mm$ in G_z, $4.54mm$ in G_y and $5.46mm$ in G_x. The average length of the coils in the x-direction is about $18mm$. The gradient set was constructed from a solid Vaspel cylinder, which had grooves precisely milled into it. Wires were carefully wrapped onto this cylinder and then potted in Epoxy to prevent motion. The final coil set is entirely contained within a $18mm$ long cylinder with a $14mm$ outer diameter and $5mm$ inner diameter. Compared to the more common large shielded gradient coils, these small coils have much higher efficiency, less eddy currents, and shorter switching time. However, these coils will induce certain eddy currents that will last longer than the desired gradient pulse. The time constants are about $10\mu s$ for G_z and G_y, and $20\mu s$ for G_x. Fortunately, they are very short compared to the spin-spin relaxation time and the gradient pulse length in most microscopy experiments ($> 500\mu s$). A short delay before detection will eliminate the eddy current effects, therefore, no distortion observed.

The calculated coil efficiencies are $80G/(cm \cdot A)$ for G_z, $55G/(cm \cdot A)$ for G_y, and $30G/(cm \cdot A)$ for G_x. The uniformity inside the volume of interest, a $2mm$ long cylinder with a diameter of $2mm$, is summarized in table 4.2.

gradient coil	efficiency (measured)	resistance	deviation
Gz	$84G/(cmA)$	0.27Ω	$< 0.5\%$
Gy	$51G/(cmA)$	0.36Ω	$< 0.5\%$
Gx	$27G/(cmA)$	0.40Ω	$< 0.5\%$

Table 4.2: Gradient coils.

64

Duty Cycle

In fast repeating or long experiments, which are the usual cases in NMR microscopy, the heating of the gradient set is an important factor. The melting temperature for wires, solder, and epoxy are considerably high. It is the break down point of insulation coating ($180^o C$) that sets the maximum duty cycle. The resistance of each coil was measured. Based on these, the heat generation in each coil at current $15A$ and the time for insulation breakdown under a continuous power supply are calculated. In this calculation, it is assumed that the heat generated is accumulated in coils with no heat transfer to the surrounding. A constant current of $15A$ brings the temperature up to $180^o C$ in about 1 second. This calculation is rough, but it provides the right order of magnitude. The vaspel former and teflon holder are considered heat resistant materials. Radiative heat transfer is negligible at this temperature range (from $4^o C$ to $180^o C$). Chilled air is blown into the probe continuously, which keeps the surrounding temperature $4^o C$. In practice, the duty cycle of the gradient set is kept to less than 1% for safety. This corresponds to a repetition time of $100ms$ in most microscopy experiments.

4.1.3 Microscope Layout

The microscopy probe developed for a standard bore 14T magnet is shown in Fig. 4-2. Compared to commercially available NMR microscopes, it has the unique features of much stronger gradients, highly sensitive RF circuit, and a sample arrangement that is suitable for small tissue and living organisms. According to the results shown in Chapter 2, the equipped gradients are strong enough to achieve a resolution of $2\mu m$ along the z axis, $2\mu m$ along the y axis, and $8\mu m$ along the x axis for free water at room temperature. With the $1.0mm$ RF coil, a 3D phantom image was acquired using a basic CTI sequence with $64 \times 64 \times 16$ phase-encoding steps (Fig. 3-6). This image has a SNR around 1, and a $2\mu m \times 2\mu m \times 8\mu m$ voxel containing 2.3×10^{12} spins. Therefore, the minimum detectable number of spins after a single excitation is about 6×10^{14} with this microscope.

4.2 System Description

Fig. 4-3 shows, in block diagram format, the essential elements of the microscopy system. It is based on a standard Bruker AMX600 spectumeter. The gradient control board and interface allow the generation of shaped gradient pulse and first order gradient shimming. The Techron power supply amplifiers have a slew rate of $21V/\mu s$, which enables fast switching of gradients. Over the range of 50Hz to 25kHz, the power output is 273W r.m.s. into a 2Ω load. It corresponds to a maximum of 15A current output for these gradient coils. Fuses are placed immediately after the amplifiers to protect the gradient set. An array of lowpass filters is connected in serial to the coils to prevent RF noises. The whole system is controlled by a Silicon Graphics O_2 computer with Bruker $XWINNMR$ software package. Special matlab programs were written to reconstruct the CTI images.
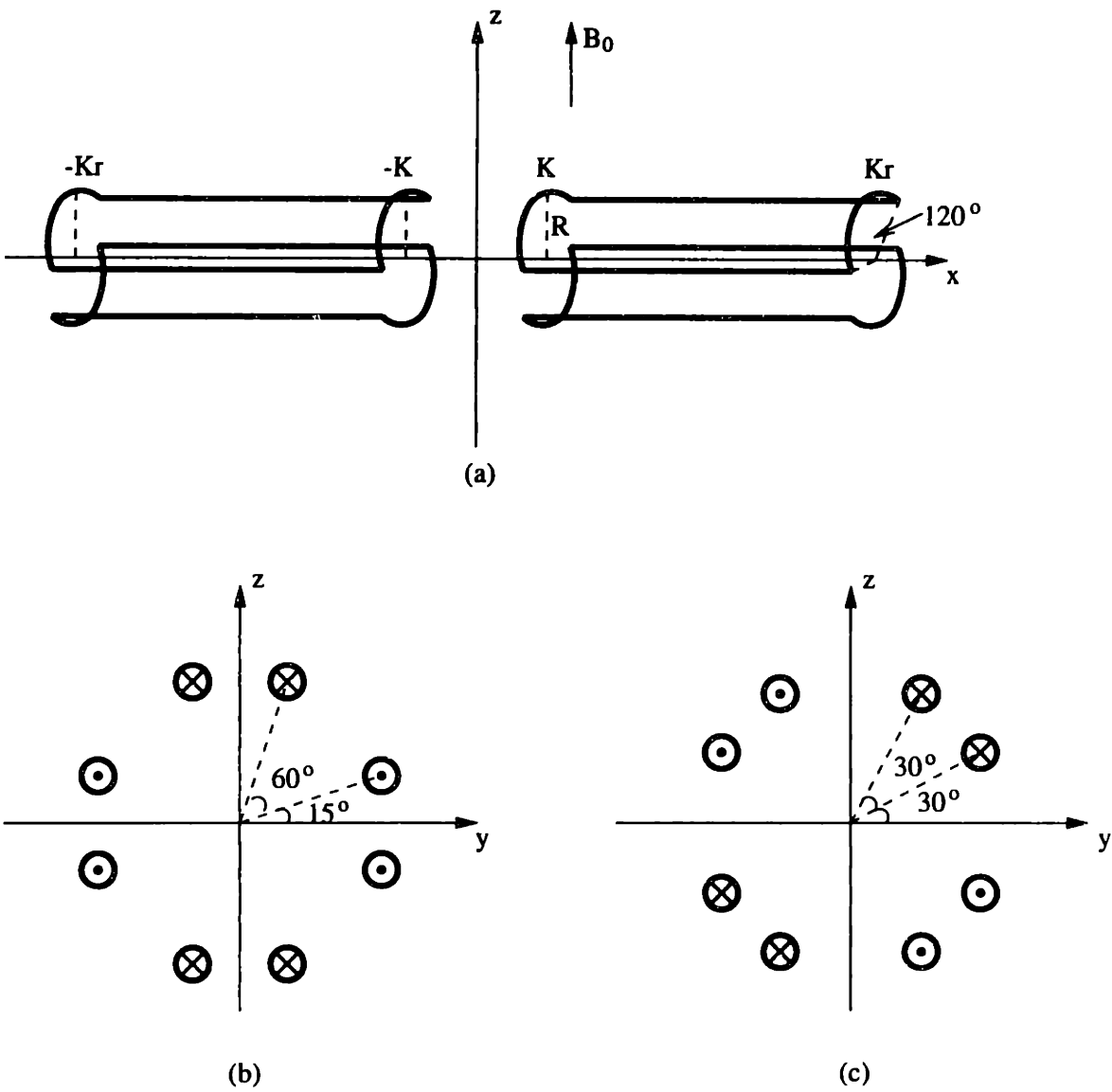
Figure 4-1: Schematic diagrams of current paths of x, y, and z gradient coils — (a) Golay coil (G_x), (b) quadruple coil (G_y), and (c) quadruple coil (G_z).
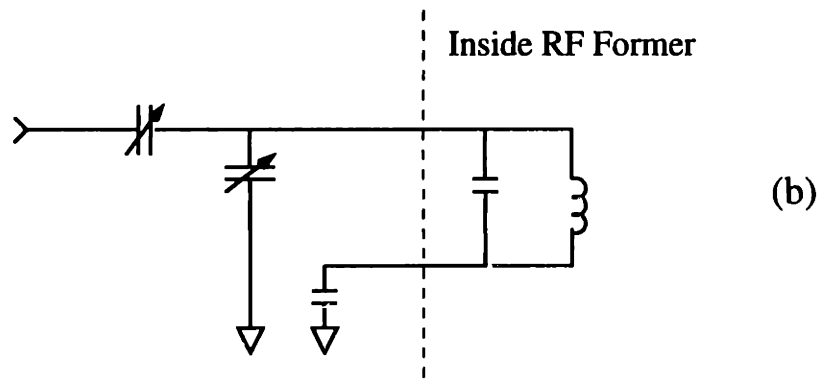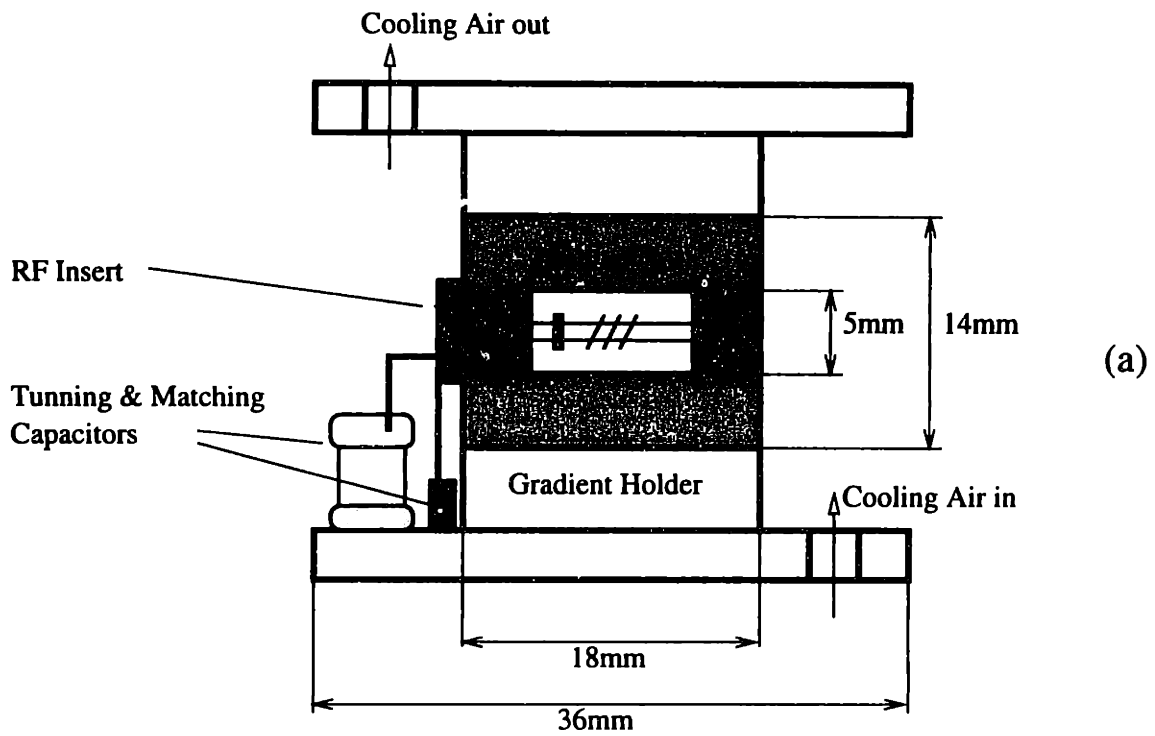
Figure 4-2: The overall layout of the NMR microscopy probe (a) and the RF circuit (b). The actual dimensions are provided. This probe is useful for samples up to 1.9mm o.d, and allows cooling up to 4^oC.
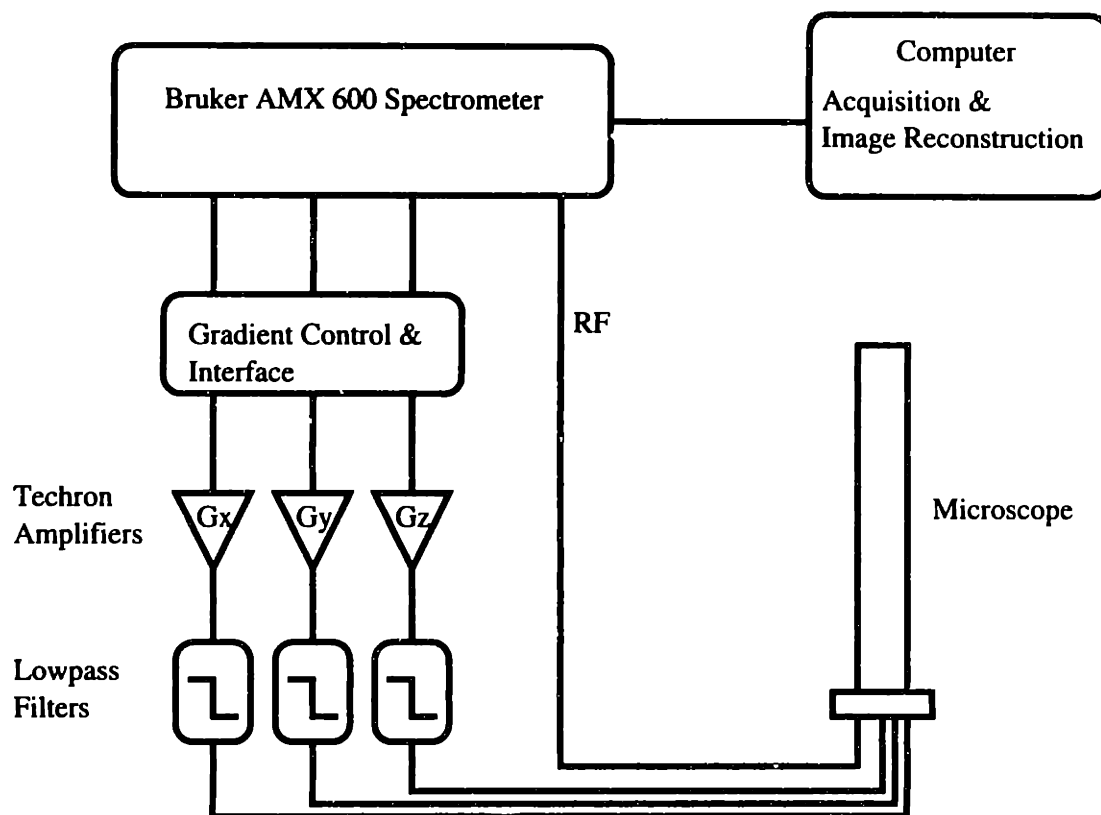
Figure 4-3: Block diagram of the microscopy system.

Chapter 5

Representative Images and Sample Applications

A wide variety of images have been acquired using the 600MHz system and the microscope described in chapter 4. Representative images are presented here to demonstrate the potential applications of NMR microscopy.

5.1 High Resolution Images

To date, the published highest resolution 3D MRI image claimed to have a resolution of $(6.4\mu m)^3$ for fixed tissue [50, 51]. It should be noted that, this resolution doesn't reflect the true physical resolution. In this study, the diffusion limited resolution was more than $20\mu m$. The following results show that this resolution can be improved to at least $2\mu m \times 2\mu m \times 8\mu m$ with a correct accounting of the diffusion limit.

Figure 5-1 shows a 3D image of a water phantom. It is a cylinder of water doped with $25mM$ $CuSO_4$. A portion of the cylinder $(100\mu m)$ was slice selected for 3D imaging. It has a T_1 of $100ms$, T_2 of $100ms$, and T_2^* of $45ms$. This image has a data size of $64 \times 64 \times 16$. It was acquired within 4 hours and 30 minutes with a FOV of $(128\mu m)^3$. Since T_2^*/T_2 is approximately 0.5, the optimal imaging sequence is CTI with single echo multi-point detection. A total number of 20 points after each excitation were acquired for signal averaging. The overall SNR in this image (average

signal amplitude over the r.m.s. of the noise) is about three (Fig.5-2).

Figure 5-3 displays all the slices in a 3D image of a Drosophila embryo. Adult flies laid eggs on a fresh Petri dish of yeast-glucose-agar medium seeded with live yeast overnight. Then the eggs and yeast were washed away from the surface of the medium using a water stream. A simple filter made from nylon mesh retained the eggs but not the yeast cells. A single egg was then mounted into a capillary tube and immediately imaged. The whole image was acquired in $5hours$ and $33minutes$ with a repetition time of $300ms$. It has a resolution of $4\mu m \times 4\mu m \times 32\mu m$ and a FOV of $256\mu m \times 256\mu m \times 512\mu m$. Four echo CP coherent detection was used with 8 points detected per echo. The phase encoding period and echo time were $383\mu s$ and $4.6ms$. A detection bandwidth of $2000Hz$ was used, which covered both the resonance peaks from water and lipid. The intensity in the images corresponds to the cell density inside the embyo. Gastrulae are observed.

5.2 Application to Developmental Biology

A great potential of NMR microscopy is for the study of small living creatures, such as Drosophila Melanogaster (fruit fly). Compared to other microscopy techniques, NMR microscopy has enormous advantages:

1. It allows one to obtain 3D information of an opaque object without dissectioning. There is practically no sample preparation necessary besides anesthesia.

2. There is no inference with subsequent histologic studies.

3. It allows the study of the same organism at various time points in its life cycle, and thus provide valuable developmental information.

4. Image contrast can be based on a variety of NMR parameters such as proton density, spin-lattice relaxation time, spin-spin relaxation time, and diffusion coefficient. Therefore, NMR microscopy can provide new information about local chemistry, morphology, and spin transport.

Here 3D images of Drosophila Melanogaster are presented. It is a little insect about 2mm long and 1mm in diameter. Drosophila has been used as a model organism for research for almost a century, and today, is widely used in gene replacement studies. It's importance for human health was recognized by the award of the Nobel prize in medicine/physiology to Ed Lewis, Christiane Nusslein-Volhard, and Eric Wieschaus in 1995. There is a major effort underway to map and sequence the entire Drosophila genome [43]. So far, about 90% of the genome has been sequenced, but only 30% has been systematically mapped. More recently, Drosophila has been used in developmental biology, looking to see how a complex organism arises from a relatively simple fertilized egg [42, 47]. There is a great deal of interest in the embryonic development and in how various adult structures, such as compound eyes, develop from imaginary discs [38, 14, 26, 5].

5.2.1 Lifecycle

Fly development proceeds through four distinctive stages: embryo, larva, pupa, and adult fly. The stages are identified by the events taking place and the time after fertilization at which they occur. Figure 5-4 shows the time in hours after the eggs are laid for the different developmental stages at room temperature (25^oC). It should be noted that the Drosophila life cycle is very sensitive to temperature. Therefore, it is possible to extend the time course of each stage deliberately to a period long enough for NMR imaging experiments.

The stage of embryo lasts about 21 hours at 25^oC and 41 hours at 18.5^oC. Provided that NMR microscopy has the sufficient temporal ($\sim hours$) and spatial (a few microns) resolutions, as demonstrated in Fig. 5-3, it will help to answer many questions about the gastrulation and morphogenetic movements during embryo development.

Drosophila larvae undergo two moults. The first and second instars last about 24 hours, and the third about 48 hours. Figure 5-5 shows a 3D image of a 2nd instar larva. It was acquired using the standard 3D spin warp sequence. This image gives a water density distribution free of artifact.

The stage of pupa lasts about 440 hours. Cells undergo growth and morphogenetic movement until at last they sculpture the adult fly. A lot of interest has been attracted to a better understanding of the metamorphosis occurs during this period. Practically, there is no sample preparation needed for NMR imaging experiments of the pupae.

Figure 5-6 shows a volume rendered 3D H^1 image of a wild type adult Drosophila. It was acquired in 1 hour and 42 minutes with a short repetition time of $500ms$. By varying the repetition time and echo time, we were able to introduce T_1, T_2, and diffusion contrasts into the images. With T_1 contrast, the central nervous system has much higher signal intensity than the surrounding fluid and fat. Almost all the major structures of an adult brain are well resolved (Fig.5-7), the muscle groups underneath the wings are identified as a dark region (Fig.5-8), and the reproductive system can be recognized in T_2 weighted images (indicating that it has a relatively long spin-spin relaxation time) (Fig.5-9). Figure 5-10 gives a comparison between images with different contrast mechanisms. T_2 weighting not only creates a contrast between the central nervous system and the surroundings, but also provides contrast among the structures inside the nervous system. In order to introduce T_2 weighting, a relatively long spin echo time of $10.5ms$ was used. Inevitably, diffusion was also a contribution to the overall contrast.

The above images (Fig. 5-3,5-5,5-6) demonstrate that NMR microscopy is well capable of following the morphological changes in the different developmental stages of fruit fly, suggesting that NMR microscopy will be a power tool for morphogenetic and embryogenetic studies.

5.2.2 Mutations

In 1982, Prof. Gelbart's group (Department of Molecular & Cellular Biology, Harvard) intentionally modified a portion of the decapentaplegic gene complex (dpp) of the fruit fly and studied the mutants with electron microscopy externally [45]. The dpp mutant individuals can be divided into six phenotypic classes. Based on these phenotypes, they suggested that the dpp gene complex is involved in the elaboration of positional information within developing epidermal tissue. They kindly provided

us a few class III mutants for pilot experiments. Class III is the most frequently encountered class of dpp mutations.

Figure 5-11 shows the 3D surface rendered H^1 NMR images of both wild type (a) and mutated (a) adult drosophila (head portions only). The flies were prepared and imaged under the exactly same conditions. Each fly was imaged as a whole. The outer surface (semitransparent) outlines the shape of the head. The inner surface (opaque) outlines the nervous system inside. The contrast between these two areas is achieved using T_1 weighting as described above. The class III dpp mutants have a much smaller head and dramatically different internal structures as expected. Figure 5-12 shows the representative slices taken from the 3D images shown in figure 5-11. The mutant fly has a significantly larger antennal lobe (fig. 5-12d) than that of a wild type drosophila (fig. 5-12a). This is consistent with the observations by electron microscopy. The class III mutants have a third antenna segment developed on the base of a normal arista. The compound eyes of a wild type drosophila are composed of over 700 ommatidia. But the class III mutant only produces 100 ommatidia or less. This dramatic difference in eye size is well demonstrated in Fig. 5-12b & e. Comparing Fig. 5-12c & f, it is clear that the mutated fly has a reduced optical lobe, including medular and lobular. This is an example of the kind of information that can not be retrieved by light or electron microsocpy without dissectioning.

The sample preparation is quite simple. Each fly was put into a petri dish together with a chloroform doped cotton ball. In less than a minute, the fly was dead and mounted into a 1mm capillary tube and ready for experiments. Still, there is a lot to learn about handling the flies. In future studies, the fly will be kept alive and anesthesia by lowering the temperature. Each image was acquired in 1 hour 42 minutes, and has a isotropic resolution of $(28\mu m)^3$. Those images are T_1 weighted. The signal from the surroundings (fluid and fat) outside of the nervous system is compressed since they have relatively long T_1.

These results suggested that NMR microscopy will be especially valuable in investigating the internal structure of mutations resulted from targeted gene replacement or other gene modification techniques. It is well suited to follow minor morphological

changes of the internal structures such as optical bundle and reproductive system, and it is uniquely capable of providing information about physiological changes in tissue.
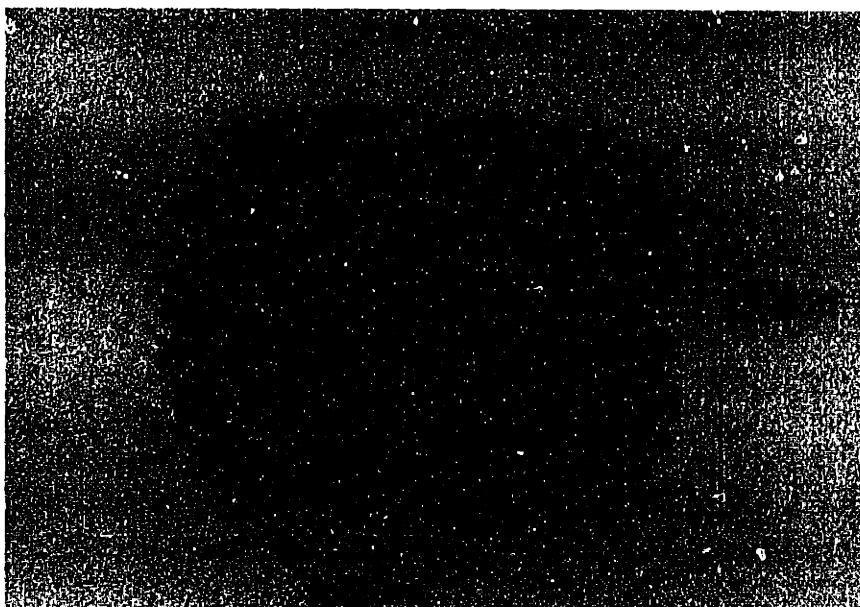
Figure 5-1: 3D image of water phantom.
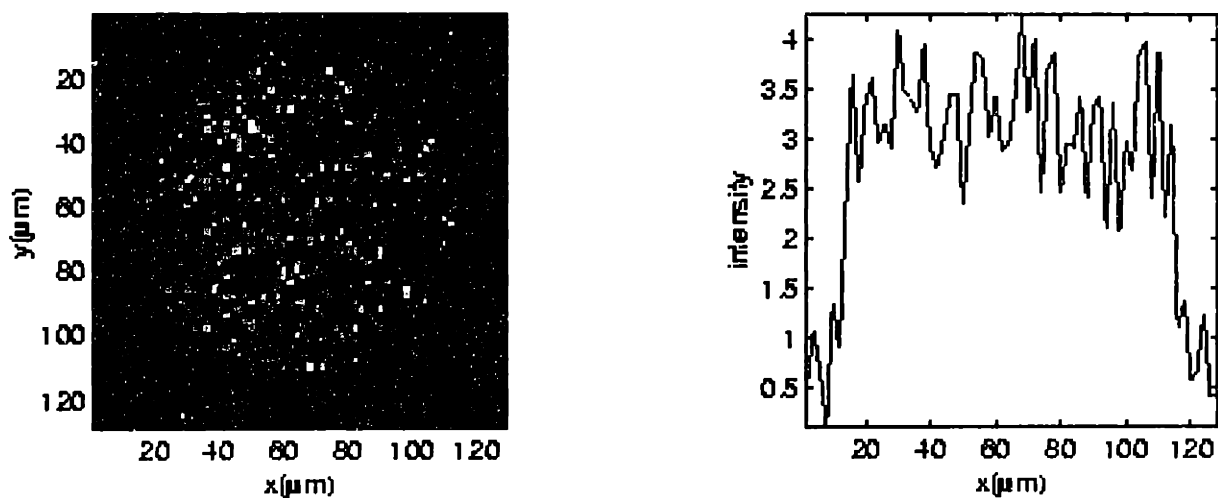
Figure 5-2: Center slice and center line plot of Fig.5-1. The SNR is about 3.
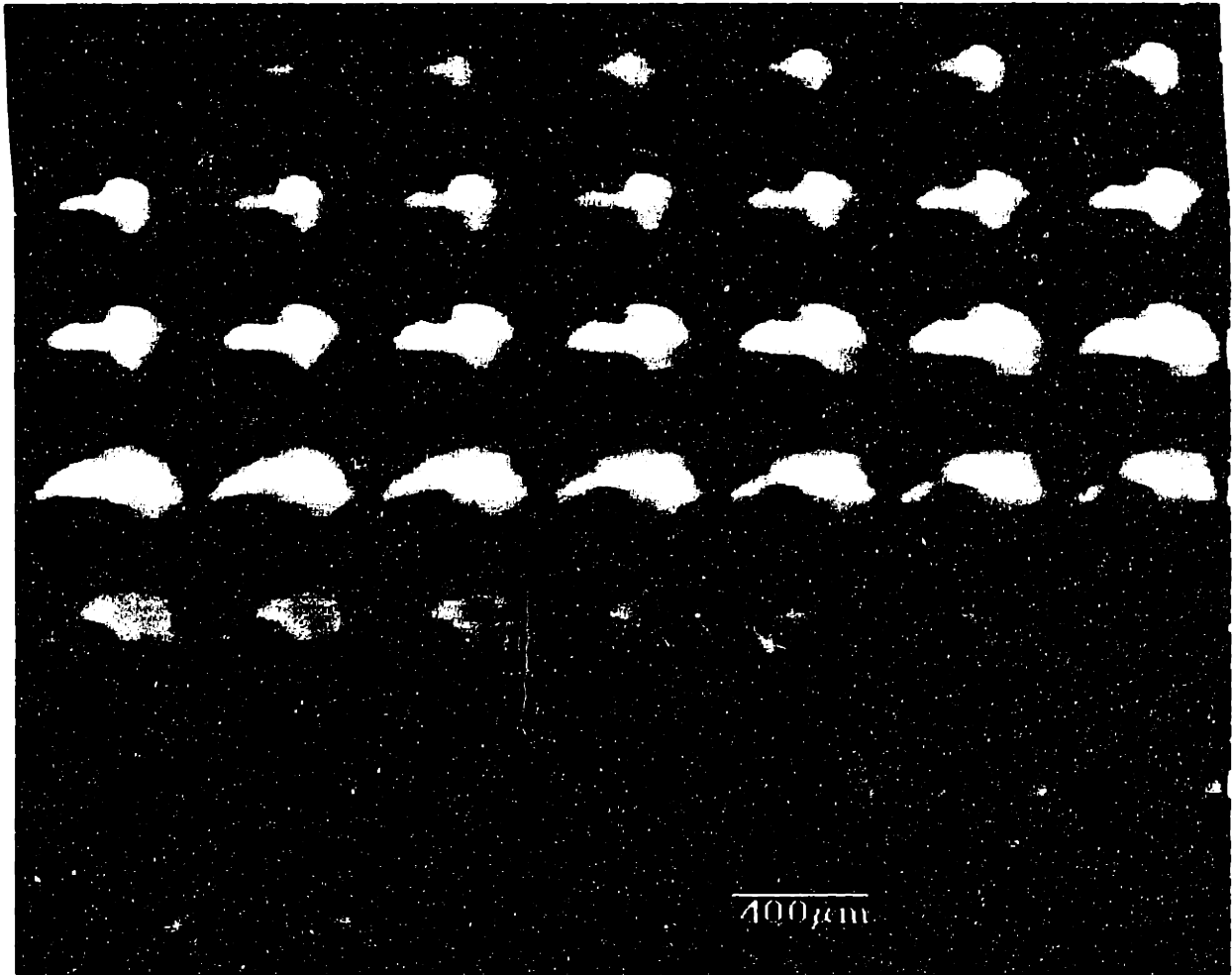
Figure 5-3: 3D H^1 image of Drosophila embryo.

Fusion of
egg and sperm → Fertilized Egg

Time (hour)

mating

courtship

Adult

Synchronized Mitoses

Embryo

Emergy of
Adult Fly — **220hr**

2.5hr— Cell Formation

Pupa   Metamorphosis

22hr — 1st Instar Larva

Larva

70hr — 2nd Larval Moult

Puparation — **120hr**
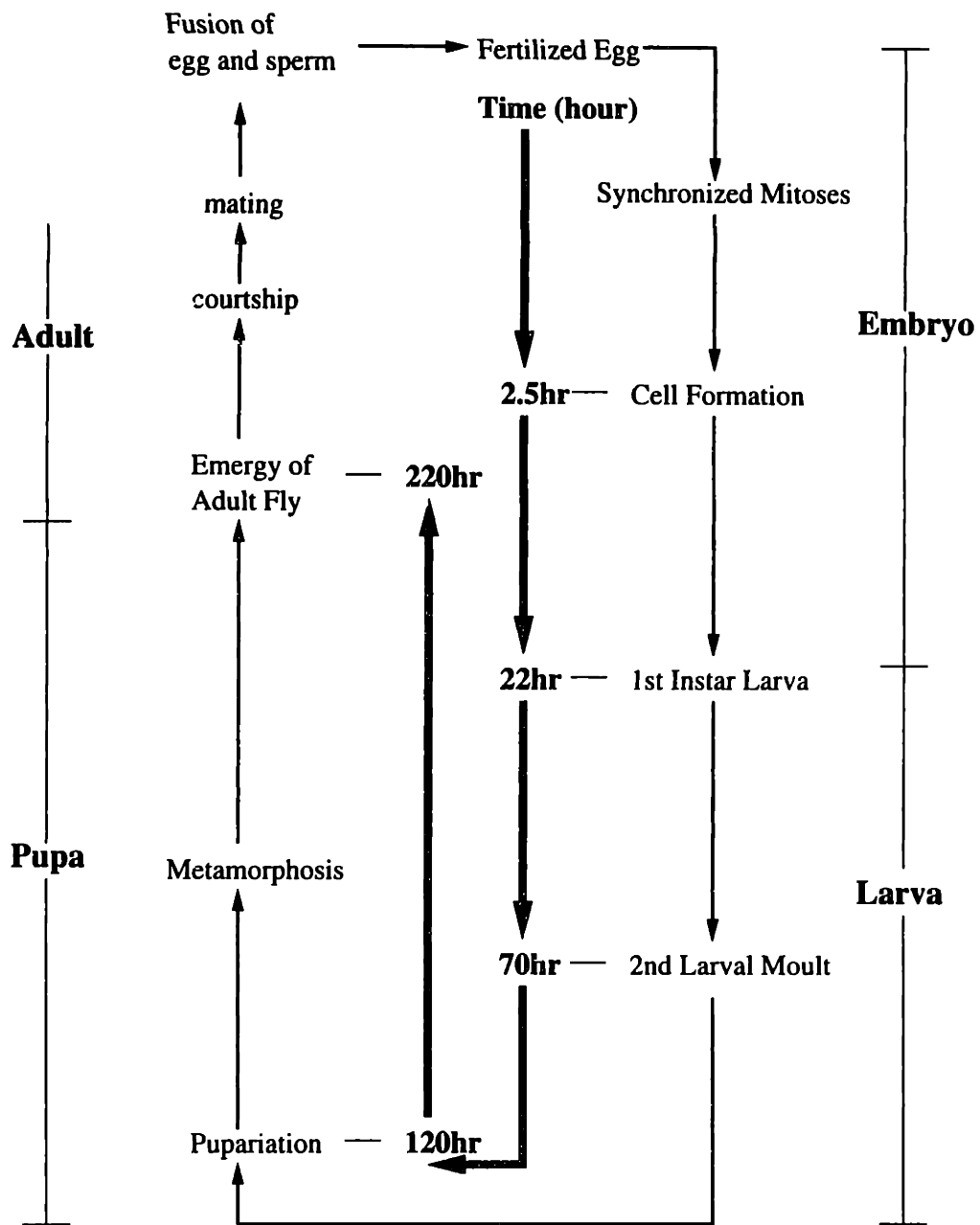
Figure 5-4: The Drosophila life cycle. All times are for 25^oC.
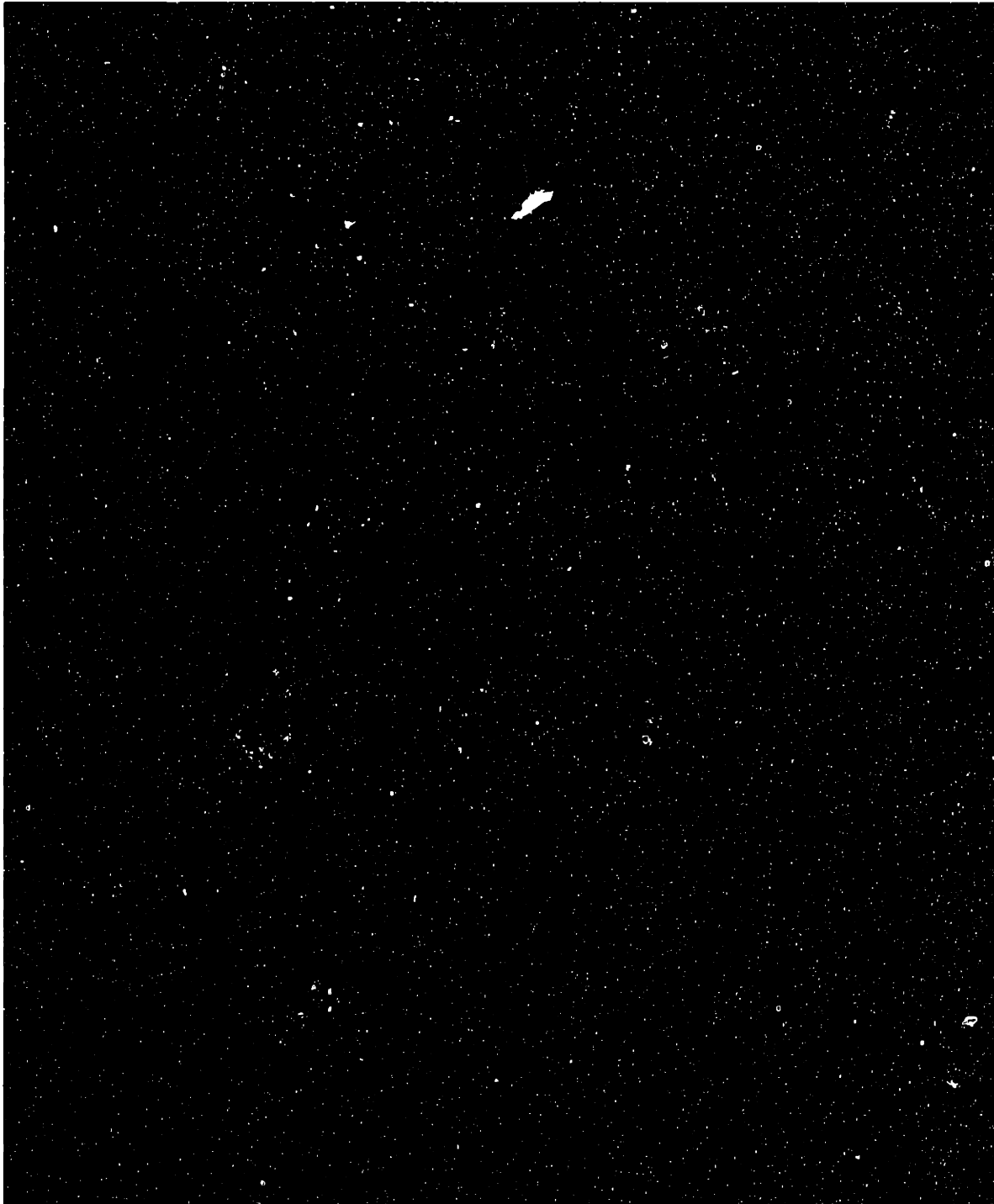
Figure 5-5: Montage display of a 3D spin echo image of a Drosophila larva (sorted from posterior to anterior). This image has an in-plane resolution of $(5.2\mu m)^2$, and a slice thickness of $100\mu m$. The total experiment time is 13 hours with 4 times signal average. It has a FOV of $1.34mm \times 1.34mm \times 3.2mm$.

Head   Thorax   Abdomen

Legs
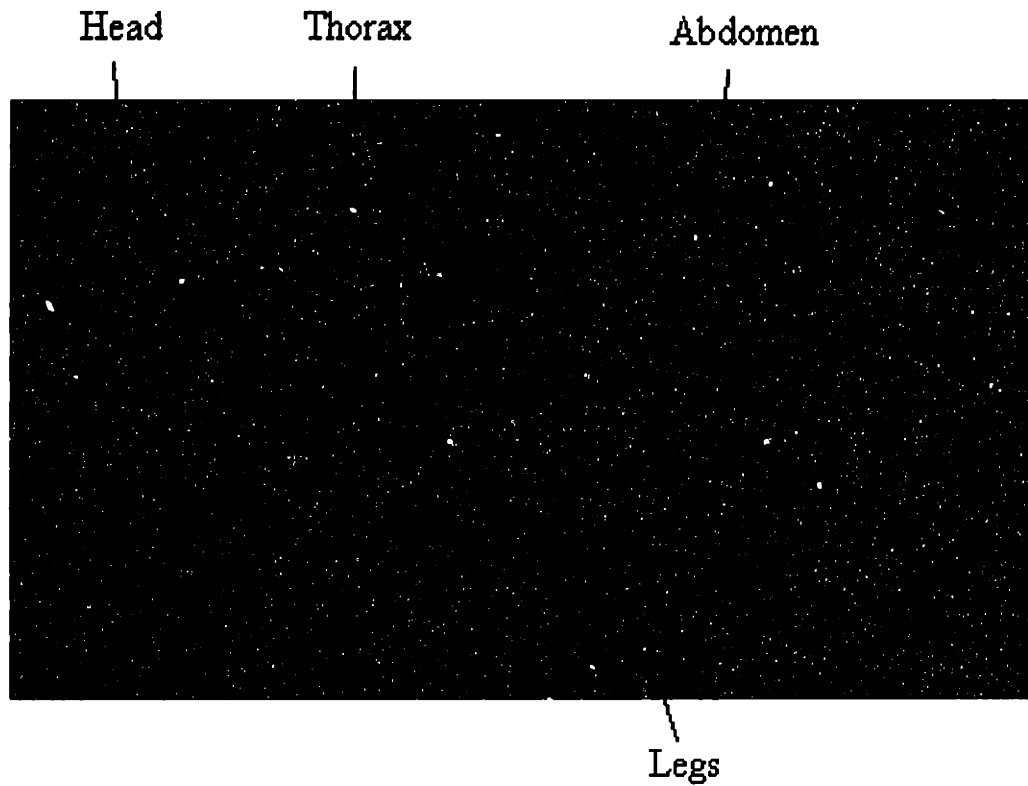
Figure 5-6: T_1 weighted 3D NMR image of a Drosophila Melanogaster adult fly. It was acquired using 3D spin echo imaging sequence. The total experimental time was 1 hour 42 minutes, with a repetition time of $500ms$ and an echo time of $2.5ms$. This image has an isotropic resolution of $(28\mu m)^3$.

(a)

(b)

Cervical
connection

Central
complex

Medulla
& lobula

Lamina

Retina

Prb   Fu
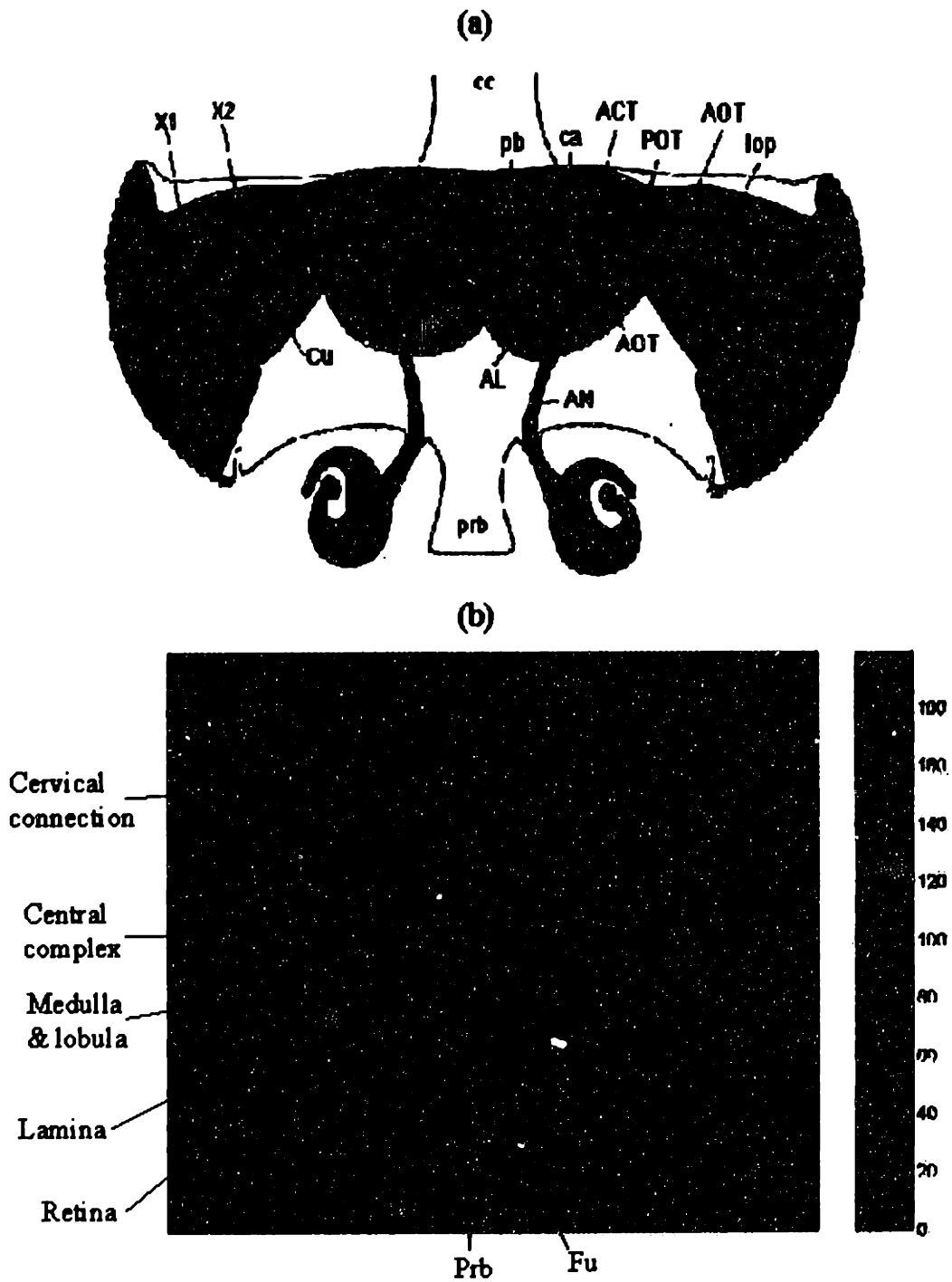
Figure 5-7: A horizontal section of a Drosophila Melanogaster adult brain. (a) Schematic drawing. (b) NMR image of the identical section with T_1 weighting. This is a slice taken from a 3D image acquired in 1 hour 42 minutes. Both the in-plane resolution and slice thickness are $28 \mu m$.
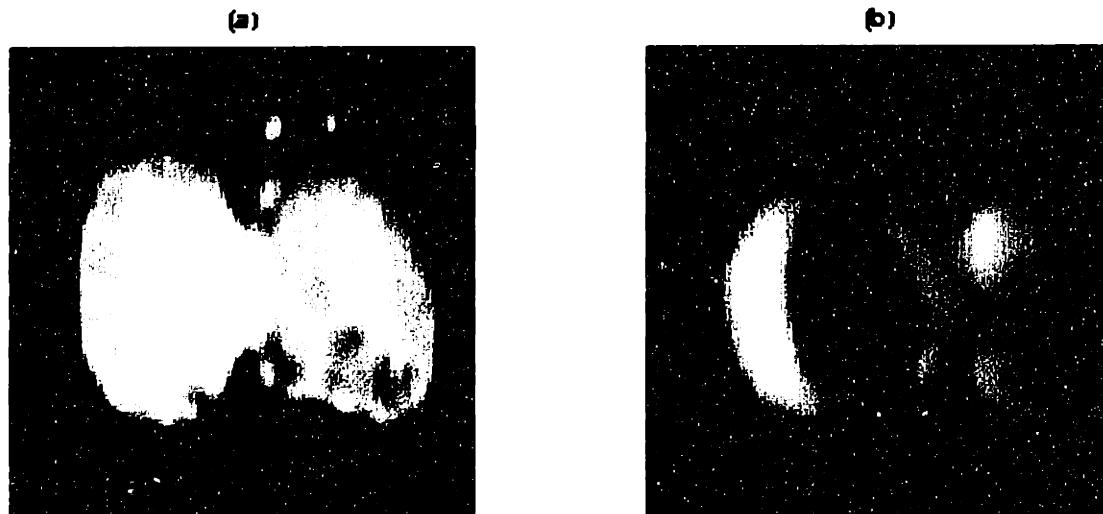
Figure 5-8: Identical slices taken from the 3D NMR images of an adult Drosophila without (a) and with (b) T_1 weighting.
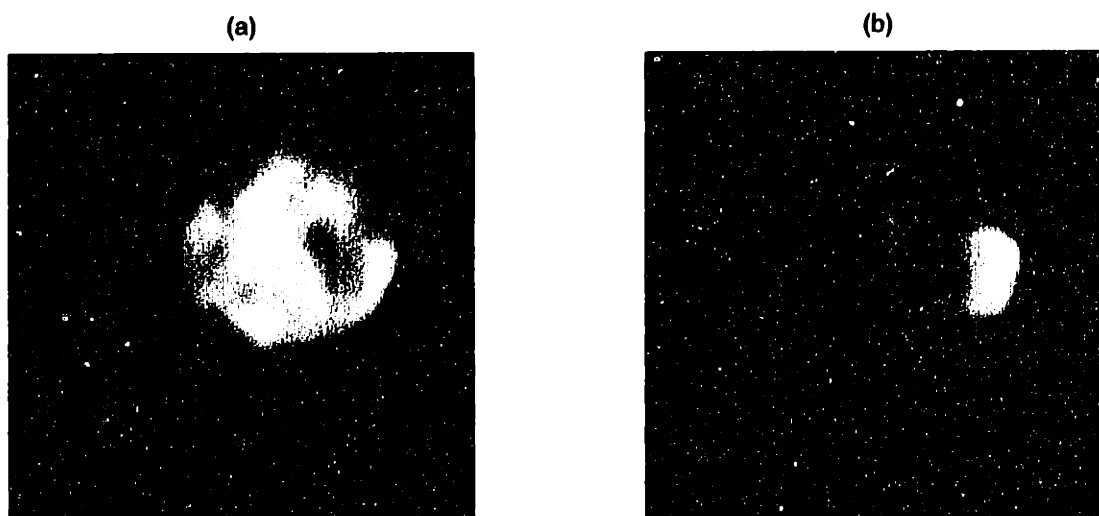
Figure 5-9: Identical cross sections of an adult fly abdomen taken from the 3D NMR images without (a) and with (b) T_2 weighting. The reproductive system is shown in (b) as a bright area.
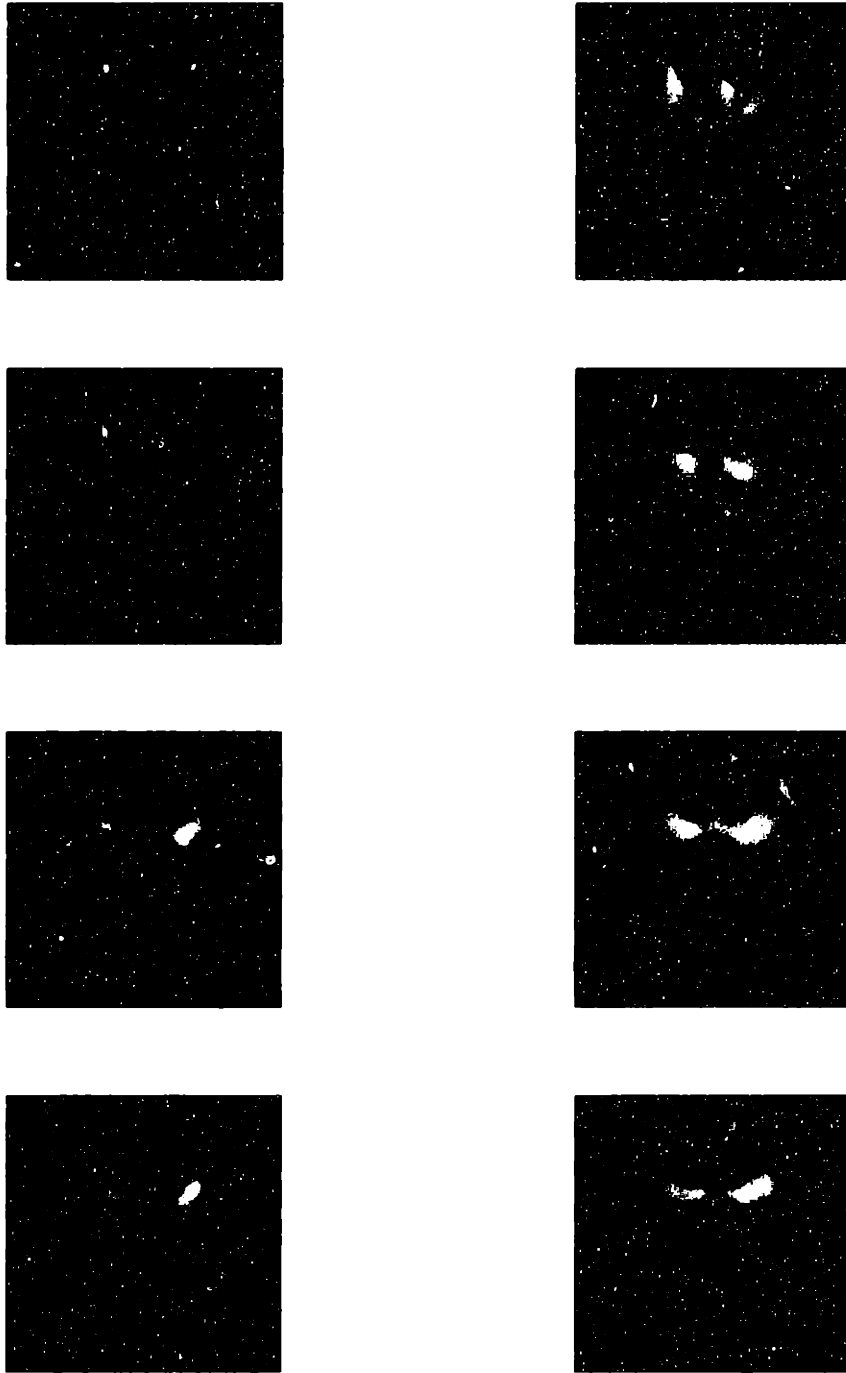
Figure 5-10: Representative brain slices taken from 3D NMR images with T_2 (left column) and T_1 (right column) weighting respectively. These two 3D images were acquired consecutively without moving the object.
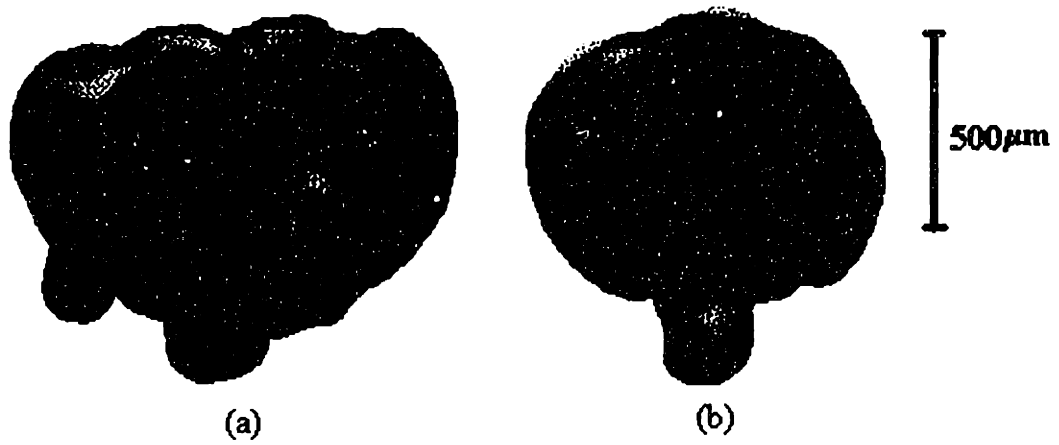
Figure 5-11: 3D H^1 image of the wild type Drosophila Melanogaster (a) and class III dpp-mutant (b). Only head portions are shown.

(a)

Antennal
Lobe

(d)

(b)

Compound
Eyes

(e)

(c)

Optical
Lobe

(f)
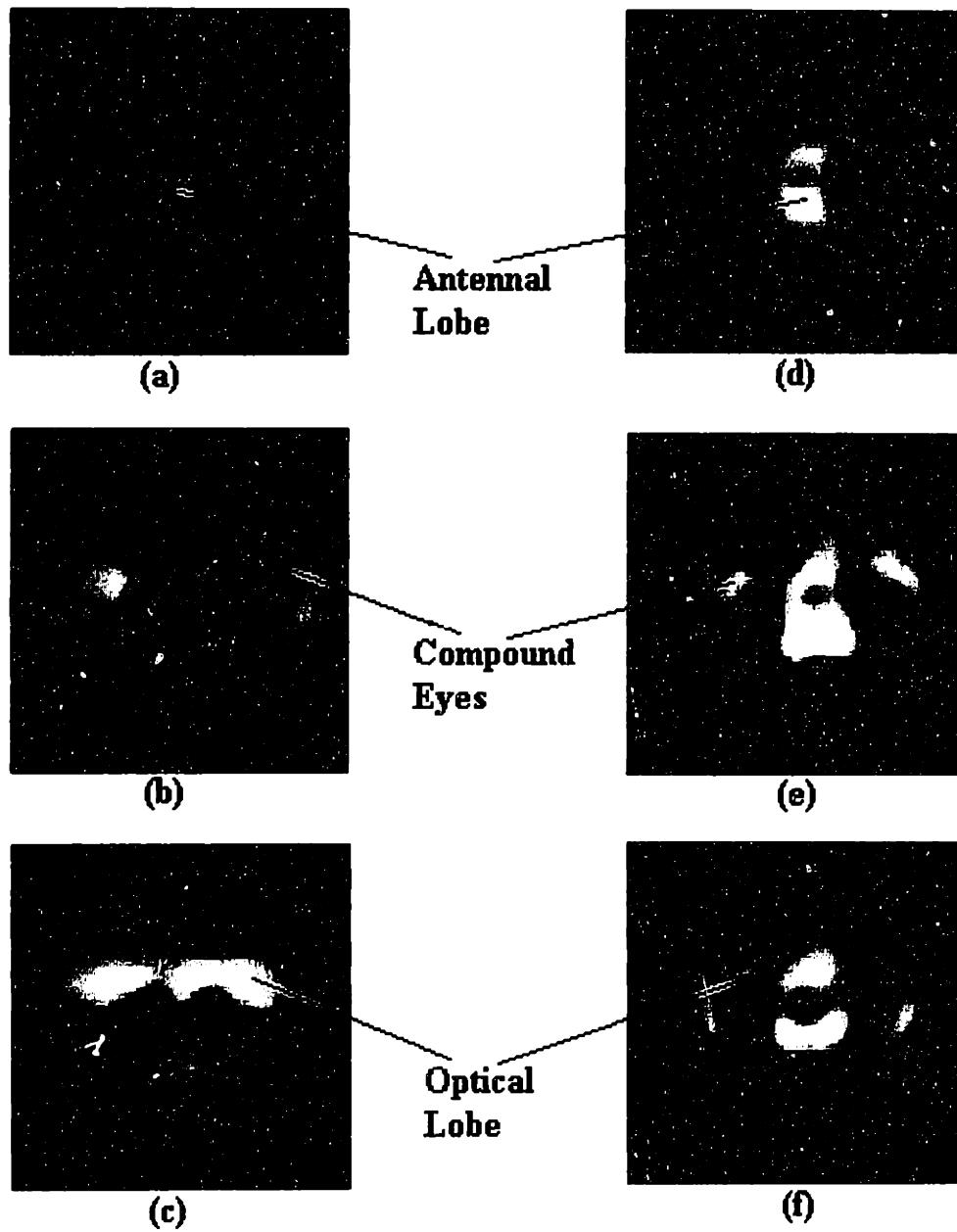
Figure 5-12: Representative brain slices taken from the 3D images shown in figure 5-11.

Chapter 6

Significance and Future Work

6.1 Significance

From the purely NMR point of view, the technological and scientific developments are themselves significant. The development of a high-resolution NMR microscope will have far reaching consequences both in terms of applications, and in terms of providing improved NMR instrumentation, and methodologies. Many of these technical improvements will have importance beyond the NMR microscopy project, and particularly in the area of high resolution NMR spectroscopy.

The NMR study of natural products is a large field which is always fighting for improved sensitivity, particularly where only trace amounts of material are available. Recently this has led to a reduction in the small sample size for natural product studies from a $5mm$ to $3mm$ o.d. tube. This reduction did bring with it an increase in sensitivity, however the increase was not that predicted by the improved filling factor. The primary reason is that manufacturers are not able to simultaneously limit the stray inductance while preserving the high resolution NMR lineshape. The RF circuit developed in this work will be directly applicable to spectroscopy probes involving microscopic samples.

Magnetic field gradients are widely employed in high resolution spectroscopy both to limit the diversity of coherence pathways, and to suppress undesired resonances (usually water). These gradients should be strong, in the case of water suppression,

should switch quickly to allow optimal sampling, and should be extremely clean to not degrade the NMR spectrum. The gradients developed are both stronger and faster switching than any used in spectroscopy, and these improvements may lead to improved gradients for spectroscopy, particularly when combined with small volume NMR circuit.

Along with the instrumentation improvement, the imaging protocols developed in this work extends the resolving capability of NMR imaging down to a few micrometers. The resolution achieved, in terms of voxel size, is an order of magnitude better than the highest resolution ever published. Consequently, it will permit exciting new applications in a variety of research areas, such as pathology, drug development, targeted gene replacement, and neurosciences.

As a whole, the $600MHz$ microscopy system permits the study of small model systems such as excised tissue and cell spheroids. We believe this type of studies will significantly improve the understanding of some biochemical processes at the cellular level, which may be the origin of contrasts in human MRI. On the other hand, NMR imaging at this high resolution may also provide direct verification to the theoretical models for magnetization transfer and water motions (diffusion and perfusion) in biological tissues.

6.2 Future Work

6.2.1 Microscope Improvement

To make NMR microscopy a more versatile analytical tool, microscope improvement is always the key issue. It largely determines the type of NMR experiments possible, the type and size of samples suitable, and the information achievable on a system.

Perfusion System

One great potential of NMR microscopy is to perform complete three-dimensional histological and dynamic studies of small tissues or cell clusters. In these studies, it

is rather important to regulate the biochemical environment and stabilize the object inside the sample tube. By attaching a perfusion circuit to the developed microscope will greatly extend the capability of our microscopy system.

Numerous perfusion circuits have been independently developed over the past few years. However, all of them are designed for a vertical alignment (according to my knowledge). Most of the difficulties will arise from the engineering aspects. The pipes must fit in the very limited space inside the probe. The junctions must be properly sealed and enable convenient exchange of sample tubes. Means of protection must be considered to prevent (at least minimize) the damage of magnet and probe resulted from perfusate leaking or flooding. Proper temperature control and oxygenation of perfusate are essential characters of a perfusion system. They must be characterized imperatively. There are also other issues related to the confinement and immobilization of samples.

Multi-Channels

A microscope with multi-channels (P^{31}, C^{13}, etc.) would dramatically enrich the information content achievable in NMR experiments. P^{31} magnetic resonance spectroscopy (MRS) has long become a tool of choice for investigating muscle energetics. It has a great potential in the physiopathological study of neuromuscular diseases. Further more, the conjunction of NMR imaging, P^{31} MRS, and C^{13} MRS, which gives information about glycogen metabolism, will provide invaluable information that is not achievable by any other techniques or any of these methods alone.

However, the RF circuit will be much complicated by introducing multi-channels. A great deal can be learned from the existing multi-channel spectroscopy probes. But the horizontal alignment and small sizes of the RF coil and gradient set will raise new questions in RF circuit design.

6.2.2 Contrast Mechanisms

It is a remarkable physiological fact that all soft tissues, except for brain, are close to 80% water. Therefore, if an NMR proton density image were constructed, in which pixel intensity is proportional to mobile tissue water distribution, there would be little contrast between adjacent tissues or regions of interest. And the image would be of limited utility. At high field, the signal-to-noise ratio is increased because of the $\omega^{7/4}$ dependence. But the contrast produced by relaxation tends to be less than that at low field. Means of contrast enhancement including administration of contrast agents must be investigated to improve the quality of micro-images. The versatility of image contrasts is one of the non-dispensable and competitive advantages of NMR imaging. On the other hand, it has been demonstrated that *in vitro* results of contrast mechanisms can be directly extrapolated to *in vivo* clinical MRI [27].

NMR is a fine means of measuring molecular transport, and this introduces the possibility of directly measuring the transport of water throughout the cellular, interstitial, and vascular space. At this high spatial resolution, we hope to explore the mobility of water and metabolites through membranes and interstitial spaces, which has profound implications for contrast mechanisms in whole body MRI.

About one-half of clinical MRI involves administration of contrast agents, which implies their importance in diagnostic imaging. The majority of agents in use today are still blood-pool agents; this is the present state of art. There are additional possibilities, including lipid-specific agents that attach to myelin and other membranes, agents for in-vivo spectroscopy, and tumor-specific agents. In all these cases, it is anticipated that in vitro studies will be the first step toward understanding and predicting the behavior of these agents in the MRI context.

6.2.3 Applications to Developmental Biology

With present instruments and resolution, we believe that NMR microscopy has a potentially exciting role to play in studies involving the macroscopic movement of cells or cellular aggregates. In particular, the noninvasiveness of NMR microscopy

combined with the unique nature of NMR contrast will provide new and important insights in the areas of embryogenesis and metamorphysis. Collaborations with experts in developmental biology and genetic will be established to pursue new projects concerning biologically significant problems.

6.2.4 Functional Microscopy

Probably the most exciting recent development in MRI is the ability to obtain functional maps which depict regions of the human brain that are activated during the performance of a specific task, so called functional MRI. While functional MRI permits the investigation of integrated effects of brain functions, functional microscopy will permit the studies of information transfer on the single neuron basis. More importantly, most functional MRI studies to date are indirect, in which cerebral blood volume, flow, and oxygenation related to neuronal activity are measured. Functional microscopy will provide the possibility to study the fundamental aspects of neural response, such as ion flow, and information transport.

The realization of functional microscopy largely depends on the instrumentation and imaging protocol development. Not only the spatial but also the temporal resolution are critical. Electrode stimulation of brain slice is very reproducible and robust. One possible solution to study short term responses is to sychronize the imaging pulses and simulations electronically.

Other topics such as changes in the oxygen gradient during radiation exposure of tumor spheroids and in liver cells during exposure to toxic agents will also be great interest in future microscopy studies.

Appendix A

Sample Pulse Programs

```
; xtim.cti3dXYm
; 3D constant time imaging with no slice selection
; multi-echo, multi-points
; XY based echo train
; XY-4, phase (xyxy)
; XY-8, phase (xyxy yxyx)
; XY-16, phase (xyxy yxyx -x-y-x-y -y-x-y-x)
d20=3u;
d10=dw-d20;
d11=de;
d3=dw*l10+d11-d2;
d1=200m-d11-d2-(d11+d2+d3)*(2*l11+1);
1    ze
2    d1
     5u ph0 adc                                          ;ADC on
3    5u:ngrad
     d2
     5u:ngrad
     d1 hl1
     d11:e
     p1:e ph1                                            ;hard 90
     d11:e
     5u:ngrad                                            ;phase grd
     d2
     5u:ngrad
     d3:e
4    p2:e ph2^                                           ;hard 180x,y
     5u:ngrad:e                                          ;spoil grd
     d11:e
```

```
      5u:ngrad:e
      d11:e
  5   d20:x
      d10
      d20:x
      d10
      lo to 5 times l10                            ;l10= # points each echo
      5u:ngrad:e                                            ;spoil grd
      d11:e
      5u:ngrad:e
      d11:e
      lo to 4 times l11                            ;l11=# of echoes
      5u
      lo to 3 times l1                     ;l1=# of data in kspace along x
      rcyc=2 ph31
      10m wr #0 if #0 zd
      10m igrad
      lo to 1 times l2                                     ;l2=td2
      1s
      lo to 1 times l3                                     ;l3=td1
      exit
ph1=0
ph0=0
ph2=0 1 0 1 1 0 1 0
ph31=0
```

Appendix B

Sample Gradient Program

```
loop l3 ⟨3D⟩
    {
    loop l2 ⟨2D⟩
        {
        loop l1 ⟨1D⟩
            {
            {(8) | (0) | (0)}
            {(0) | (0) | (0)}
            {(8)+r1d(59.84) | (0),r2d(88.37) | (0),,r3d(41.4)}
            {(0) | (0) | (0)}
            loop l11
                {
                {(8) | (0) | (0)}
                {(0) | (0) | (0)}
                {(8) | (0) | (0)}
                {(0) | (0) | (0)}
                }
            }
        }
    }
```

Appendix C

Matlab Files for Image Processing

```
%read in
Nx=64;
Ny=64;
Nz=32;
Npoint=4;
Necho=8;
Sp=1;
Ep=4;
N=Nx*Npoint*Necho*2;
n=ceil(N/256);
fid=fopen('f : \cti3d9', 'r', 'b')
for k=1:Nz,
    ser(:,:,k)=fread(fid,[n*256 Ny], 'int32');
end
fclose(fid)

    % seperate real and imaginary data
SER=zeros(N/2,Ny,Nz);
for k=1:Nz,
    for l=1:Ny,
        SER(:,l,k)=ser(1:2:N,l,k)+ser(2:2:N,l,k)*i;
    end
end
clear ser

    %baseline correction
n=round(N/32);
for k=1:Nz,
    for l=1:Ny,
```

```
            bkgd=mean(SER(N/2-n+1:N/2,l,k));
            SER(:,l,k)=SER(:,l,k)-bkgd;
        end
end


    %phase correction & sum up points with same k
xc=Nx/2+1;
yc=Ny/2+1;
zc=Nz/2+1;
pha=angle(SER((xc-1)*Npoint*Necho+1:xc*Npoint*Necho,yc,zc));
SER1=zeros(N/2,Ny,Nz);
SER2=zeros(Nx-1,Ny-1,Nz-1);
for k=2:Nz,
    for l=2:Ny,
        for m=2:Nx,
            SER1((m-1)*Npoint*Necho+1:m*Npoint*Necho,l,k)
            =SER((m-1)*Npoint*Necho+1:m*Npoint*Necho,l,k).*exp(-i.*pha);
            for ne=1:2:Necho,
                SER2(m-1,l-1,k-1)=sum(SER1((m-1)*Npoint*Necho+(ne-1)*Npoint+Sp:
                (m-1)*Npoint*Necho+(ne-1)*Npoint+Ep,l,k))+SER2(m-1,l-1,k-1);
            end
            for ne=2:2:Necho,
                SER2(Nx-m+1,Ny-l+1,Nz-k+1)=sum(SER1((m-1)*Npoint*Necho+
                (ne-1)*Npoint+Sp:(m-1)*Npoint*Necho+(ne-1)*Npoint+Ep.l,k))
                +SER2(Nx-m+1,Ny-l+1,Nz-k+1);
            end
        end
    end
end
clear SER1


    %DC correction
for k=1:Nz,
    for l=1:Ny,
        bkgd=mean(SER2(1:10,l,k));
        SER2(:,l,k)=SER2(:,l,k)-bkgd;
    end
end


    %EM or Qsine multiplication
px=Nx/pi;
py=Ny/pi;
pz=Nz/pi;
for k=1:Nz-1,
    for l=1:Ny-1,
```

```
%qsine=(sin([pi*(Nx-1):-pi:0]/Nx)*sin((l-1)*pi/Ny)*sin((k-1)*pi/Nz)).^2;
%SER2(:,l,k)=SER2(:,l,k).*rot90(qsine);
EM=exp(-abs([Nx/2-1:-1:-Nx/2+1])/px)*exp(-abs(l-Ny/2)/py)*exp(-abs(k-Nz/2)/pz);
SER2(:,l,k)=SER2(:,l,k).*rot90(EM);
    end
end

    % Fourier transform
SIx=64;
SIy=64;
SIz=32;
I=abs(fftshift(fftn(SER2,[SIx SIy SIz])));

    %shift along y
yshift=38;
Ixy=zeros(SIx,SIy,SIz);
Ixy(:,SIy-yshift+1:SIy,:)=I(:,1:yshift,:);
Ixy(:,1:SIy-yshift,:)=I(:,yshift+1:SIy,:);
I=Ixy;
clear Ixy

    %shift along x
xshift=12;
Ixy=zeros(SIx,SIy,SIz);
Ixy(SIx-xshift+1:SIx,:,:)=I(1:xshift,:,:);
Ixy(1:SIx-xshift,:,:)=I(xshift+1:SIx,:,:);
I=Ixy;
clear Ixy

    %shift along z
zshift=15;
Ixy=zeros(SI,SI,SIz);
Ixy(:,:,SIz-zshift+1:SIz)=I(:,:,1:zshift);
Ixy(:,:,1:SIz-zshift)=I(:,:,zshift+1:SIz);
I=Ixy;
clear Ixy

    %Display
obj(:,:,1,:)=I;
M=max(max(max(I)));
montage(obj/M)
```

Bibliography

[1] J. B. Aguayo, S. J. Blackband, J. Schoeniger, and M. A. Mattingly. Nuclear magnetic-resonance imaging of a single cell. *Nature*, 322:190–191, 1986.

[2] C. B. Ahn and Z. H. Cho. A generalized formulation of diffusion effects in μm resolution nuclear magnetic resonance imaging. *Med. Phys.*, 16:22–28, 1989.

[3] E. R. Andrew, A. Bradbury, and R. G. Eades. Removal of dipolar broadening of nuclear magnetic resonance spectra of solids by specimen rotation. *Nature*, 183:1802–1803, 1959.

[4] D. L. Buckley, J. D. Bui, M. I. Phillips, T. Zelles, B. A. Inglis, H. D. Plant, and S. J. Blackband. The effect of ouabain on water diffusion in the rat hippocampal slice measured by high resolution nmr imaging. *Magn. Reson. in Med.*, 41:137–142, 1999.

[5] M. Buszczak and W. A. Segraves. Drosophila metamorphosis: The only way is usp? *Curr. Biol.*, 8:R879–R882, 1998.

[6] P. T. Callaghan. *Principles of Nuclear Magnetic Resonance Microscopy*. Oxford, New York, 1993.

[7] P. T. Callaghan and S. L. Codd. Generalized calculation of nmr imaging edge effects. *Magn. Reson. Imaging*, 16:471–478, 1998.

[8] P. T. Callaghan and C. D. Eccles. Sensitivity and resolution in nmr imaging. *J. Magn. Reson.*, 71:426–445, 1987.

[9] P. T. Callaghan, L. C. Forde, and C. J. Rofe. Correlated susceptibility and diffusion effects in nmr microscopy using both phase-frequency encoding and phase-phase encoding. *J. Magn. Reson.*, B 104:34–52, 1994.

[10] Z. H. Cho, C. B. Ahn, S. C. Juh, H. K. Lee, J. H. Yi, and J. M. Jo. Nuclear magnetic resonance microscopy with $4\mu m$ resolution: Theoretical study and experimental results. *Med. Phys.*, 15:815–824, 1988.

[11] S. Choi. Nuclear magnetic resonance microscopy: Using strong field gradients and constant time imaging. Master's thesis, Massachusetts Institute of Technology, Cambridge, 1996.

[12] S. Choi, X. Tang, and D. G. Cory. Constant time imaging approaches to nmr microscopy. *Int. J. Imaging Syst. Technol.*, 8:263–276, 1997.

[13] R. M. Cotts, M. J. R. Hoch, T. Sun, and J. T. Marker. Pulsed field gradient stimulated echo methods for improved nmr diffusion measurements in heterogeneous systems. *J. Magn. Reson.*, 83:252–266, 1989.

[14] W. Du and N. Dyson. The role of rbf in the introduction of g(1) regulation during drosophila embryogenesis. *Embo. J.*, 18:916–925, 1999.

[15] S. Emid and J. H. N. Creyghton. High resolution nmr imaging in solids. *Physica*, 128B:81–83, 1983.

[16] A. N. Garroway. Magic-angle sample spinning of liquids. *J. Magn. Reson.*, 49:168–171, 1982.

[17] S. Gravina and D. G. Cory. Sensitivity and resolution of constant-time imaging. *Journal of Magnetic Resonance B*, 104:53–61, 1994.

[18] T. Gullion. The effect of amplitude imbalance on compensated carr-purcell sequences. *J. Magn. Reson. A*, 101:320–323, 1993.

[19] T. Gullion, D. B. Baker, and M. S. Conradi. New, comppensated carr-purcell sequences. *J. Magn. Reson.*, 89:479–484, 1990.

[20] U. Haeberlen and J. S. Waugh. Coherent averaging effects in magnetic resonance. *Phys. Rev.*, 175:453–467, 1968.

[21] E. L. Hahn. Spin echoes. *Phys. Rev.*, 80:580–594, 1950.

[22] D. I. Hoult. The nmr receiver: A description and analysis of design. *Progress in NMR Spectroscopy*, 12:41–77, 1978.

[23] D. I. Hoult and R. E. Richards. Critical factors in the design of sensitive high resolution nuclear magnetic resonance spectrometers. *Proc. Roy. Soc.*, A344:311–340, 1975.

[24] W. B. Hyslop and P. C. Lauterbur. Effects of restricted diffusion on microscopic nmr imaging. *J. Magn. Reson.*, 94:501–510, 1991.

[25] R. D. Kapadia, W. B. High, H. A. Soulleveld, D. Bertolini, and S. K. Sarkar. Magnetic-resonance microscopy in rat skeletal research. *Magn. Reson. in Med.*, 30:247–250, 1993.

[26] E. Knust and H. A. J. Muller. Drosophila morphogenesis: Orchestrating cell rearrangements. *Curr. Biol.*, 8:R853–R855, 1998.

[27] S. H. Koenig and R. D. Brown III. *NMR in Physiology and Biomedicine*, pages 57–73. Academic Press, 1987.

[28] G. Laicher, D. C. Ailon, and A. G. Cutillo. Water self-diffusion measurements in excised rat lungs. *J. Magn. Reson. B*, 111:243–253, 1996.

[29] L. L. Latour, L. Li, and C. H. Sotak. Improved pfg stimulated-echo method for measurement of diffusion in inhomogeneous fields. *J. Magn. Reson. B*, 101:72–77, 1993.

[30] P. C. Lauterber. *NMR in Biology and Medicine*. Raven Press, New York, 1986.

[31] P. C. Lauterbur. Image formation by induced local interactions: Examples employing nuclear magnetic resonance. *Nature*, 242:190–191, 1973.

[32] J. Link and J. Seelig. Comparison of deuterium nmr imaging methods and application to plants. *J. Magn. Reson.*, 89:310–330, 1990.

[33] W. E. Maas, F. H. Laukien, and D. G. Cory. Gradient, high resolution, magic angle sample spinning nmr. *J. Am. Chem. Soc.*, 118:13085–13086, 1996.

[34] P. Mansfield and P. K. Grannell. Diffraction and microscopy in solids and liquids by nmr. *Phys. Rev.*, B12:3618–3634, 1975.

[35] P. Mansfield and P. G. Morris. *NMR imaging in biomedicine*. Academic Press, London, 1982.

[36] E. W. McFarland. Time-independent point-spread function for nmr microscopy. *Magn. Reson. Imag.*, 10:269–278, 1992.

[37] D. L. Olson, T. L. Peck, A. G. Webb, R. L. Magin, and J. V. Sweedler. High-resolution microcoil h-1 nmr for mass-limited, nanoliter-volume samples. *Science*, 270:1967–1970, 1995.

[38] D. Pan and G. M. Rubin. Targeted expression of teashirt induces ectopic eyes in drosophila. *Natl. Acad. Sci. USA*, 95:15508–15512, 1998.

[39] T. L. Peck, R. L. Magin, and P. C. Lauterbur. Design and analysis of microcoils for nmr microscopy. *J. Magn. Reson. B*, 108:114–124, 1995.

[40] S. Posse and W. P. Aue. Susceptibility artifacts in spin-echo and gradient-echo imaging. *J. Magn. Reson.*, 88:473–492, 1990.

[41] J. R. Reitz, F. J. Milford, and R. W. Christy. *Foundations of Electromagnetic Theory*. Addison-Wesley, Reading, Massachusetts, 1979.

[42] S. Roth. Drosophila development: The secrets of delayed induction. *Curr. Biol.*, 8:R906–R910, 1998.

[43] R. P. Sear and W. M. Gelbart. The flybase database of the drosophila genome projects and community literature. *Nucleic Acids Res.*, 27:85–88, 1999.

[44] A. J. Shaka, S. P. Rucker, and A. Pines. Iterative carr-purcell trains. *J. Magn. Reson.*, 77:606–611, 1988.

[45] F. A. Spencer, F. M. Hoffmann, and W. M. Gelbart. Decapentaplegic: A gene complex affecting morphogenesis in drosophila melanogaster. *Cell*, 28:451–461, 1982.

[46] B. H. Suits and D. E. Wilken. Improved magnetic-field gradient coils for nmr imaging. *J. Phys. E: Sci. Instrum.*, 22:565–573, 1989.

[47] Y. Tomoyasu, M. Nakamure, and N. Ueno. Role of dpp signalling in prepattern formation of the dorsocentral mechanosensory organ in drosophila melanogaster. *Development*, 125:4215–4224, 1998.

[48] H. C. Torrey. Block equations with diffusion terms. *Phys. Rev.*, 104:563–565, 1956.

[49] P. Weybright, K. K. Millis, N. Campbell, D. G. Cory, and S. Singer. Gradient, high-resolution, magic angle spinning h-1 nuclear magnetic resonance spectroscopy of intact cells. *Magn. Reson. Med.*, 39:337–345, 1998.

[50] *Abstracts of the 8th Annual Meeting of the Soc. Magn. Reson. in Med.*, Amsterdam, The Netherlands, 1989.

[51] *Abstracts of the 1st International Conference on NMR Microscopy*, Heidelberg, Germany, 1991.

[52] Y. Zur and S. Stokar. A phase-cycling technique for canceling spurious echoes in nmr imaging. *J. Magn. Reson.*, 71:212–228, 1987.